university of groningen
faculty of science and engineering
kapteyn astronomical institute

Bachelor Thesis

Determining Chemical Abundances in CD-51 4628 with `iSpec`

Author:
Ilse Harmers

Supervisor:
Prof. Dr. Eline Tolstoy

July 8, 2022

Abstract

Context. Nissen and Schuster 2010 analyzed 94 dwarf stars in the solar neighborhood kinematically determined to be Galactic halo stars and concluded that the Galactic halo consists of two stellar populations: "high-α" and "low-α" stars, where α refers to the average abundance of Mg `I`, Si `I`, Ca `I` and Ti `I`. They concluded that the low-α population is most likely accreted from a dwarf galaxy whereas the high-α population belongs to an "in-situ" inner halo population, or alternatively, consists of ancient disk or bulge stars that were kinematically "heated" due to mergers with dwarf galaxies (Nissen and Schuster 2010).
Aims. Differential abundances of α and neutron-capture elements are determined for the low-α halo star CD-51 4628, which is a member of Nissen & Schuster's sample and was extensively studied at red wavelengths (480 - 680 nm), using high-resolution VLT/UVES spectra. The aim of this work is to further explore the extragalactic origin of CD-51 4628 by looking for neutron-capture elements and measuring their abundances with so far unanalyzed blue spectra (329 - 451 nm).
Methods. Making use of the spectroscopic software framework `iSpec`, we have performed an LTE abundance analysis with the equivalent width method and the synthetic spectral fitting technique over the full wavelength range of 329 - 665 nm. We have redetermined the abundances reported in Nissen and Schuster 2010 and Nissen and Schuster 2011 and extended to new (neutron-capture) elements.
Results. We have determined the differential abundance ratios of Na `I`, Mg `I`, Si `I`, Ca `I`, Ti `I`, Ni `I`, Y `II`, Ba `II`, La `II`, Nd `II` and Eu `II` with respect to Fe in the wavelength range of 330 - 451 nm. In addition, we looked for absorption lines of Os `I` and Th `II` but their abundances could not be determined in a reliable manner.
Conclusions. Comparing the abundance ratios [La/Ba], [Eu/Ba], [Mg/Fe], [Eu/Mg] and [Ba/Eu] of CD-51 4628 to literature values of Gaia-Enceladus stars, Galactic in-situ stars and stars from the satellite dwarf galaxies Sculptor, Fornax, Sagittarius and LMC, we suggest that CD-51 4628 may have been accreted from Gaia-Enceladus or from a dwarf galaxy with a mass comparable to Sculptor or Fornax.

Contents

Abstract . . . 2

1 Introduction **4**

2 Astrophysical Background **7**
2.1 Galactic Archaeology . . . 7
2.2 Slow and Rapid Neutron-Capture Processes . . . 8

3 Spectroscopy **11**
3.1 Equivalent Width Method . . . 12
3.2 Synthetic Spectral Fitting Technique . . . 14

4 Methodology **15**
4.1 UVES . . . 15
4.2 `iSpec` . . . 16
4.3 Raw Data Processing . . . 17
4.4 Determining Atmospheric Parameters . . . 20
4.5 Abundance Analysis . . . 21
4.5.1 Equivalent Width Method . . . 21
4.5.1.1 Red Spectra . . . 22
4.5.1.2 Blue Spectra . . . 22
4.5.2 Synthetic Spectral Fitting Technique . . . 23

5 Results **24**
5.1 Determining Atmospheric Parameters . . . 24
5.2 Abundance Analysis . . . 25
5.2.1 Red Spectra . . . 25
5.2.2 Blue Spectra . . . 25

6 Discussion **28**
6.1 Comparisons with Literature . . . 28
6.2 Extragalactic Origin of CD-51 4628 . . . 32
6.3 Suggestions for Further Research . . . 33

7 Conclusion **36**
Acknowledgements . . . 37

Bibliography **38**

Appendix A **43**

Chapter 1

Introduction

As a starting point, we should provide a definition for the celestial object dubbed a *star* (LeBlanc 2010):

"A star can be defined as a self-gravitating celestial object in which there is, or there once was (in the case of dead stars), sustained thermonuclear fusion of hydrogen in their core."

In the bigger picture of the Universe, stars are seen as essential building blocks of all galaxies. Thus, understanding the way these celestial objects evolve is crucial for comprehending the evolution of galaxies throughout the eons (Higl and Weiss 2017). From their spectra, it is clear that stars mainly consist of hydrogen and helium and a minor fraction of other chemical elements (Cyburt et al. 2016; LeBlanc 2010). Studying the absorption line spectra from the photospheres of stars, which is dubbed stellar spectroscopy, is therefore of utmost importance in order to understand the chemical make-up of stars, their place in a galaxy and the preceding chemical evolution of said galaxy (Higl and Weiss 2017).

For more than a century, stellar spectroscopy has played a pivotal role in our comprehension of stars and especially stellar abundance analyses, in which the relative amounts of 'interesting' chemical elements can be ascertained from the absorption line spectrum of a stellar photosphere (Aufdenberg 2003). Specifically, the works of Meghnad Saha, Cecilia Payne, Henry Norris Russell and Marcel Minnaert (to name but a few) can be considered the foundation on which modern stellar analysis is built, such that equivalent widths of stellar spectral lines could be utilized to determine the corresponding chemical abundances (Aufdenberg 2003).

As expected from stellar evolution models, stars are mainly composed of hydrogen and helium, the lightest elements in the periodic table, with an observed ratio of 3:1 set by Big-Bang Nucleosynthesis (Aufdenberg 2003; Copi et al. 1995; LeBlanc 2010). The presence of other elements in stellar atmospheres indicates, for example, with which types of supernovae the antecedent interstellar gas cloud was mainly chemically enriched (LeBlanc 2010; Nissen and Schuster 2010). Additionally, the intermittent presence of heavier neutron-capture elements ($Z > 30$) provides further clues regarding the chemical history of a star's birth site and the relative speed of its site's chemical evolution (Nissen and Schuster 2010; Sneden et al. 2008; Van der Swaelmen et al. 2016).

There have been many interesting studies of the chemical and kinematic peculiarities of Galactic and extragalactic stellar populations with the intention of distinguishing the differing populations based on their chemistries, e.g. see Carollo et al. 2007; Helmi et al. 2018; Venn et al. 2004. In particular, comparisons between the chemical signatures and kinematics of stars in the standard Galactic components (e.g., thin-disk, thick-disk and halo) and the Milky Way dwarf spheroidal satellite galaxies (dSphs) allude to the existence of at least two distinct stellar populations in the Galactic halo, as Nissen and Schuster 2010 has demonstrated using high resolution spectra and precise abundance ratios of dwarf stars with halo kinematics. Most likely, one of the populations is composed of stars that were accreted from satellite dwarf galaxies while the other could belong to an "in-situ" inner halo population which might have formed during a dissipative

collapse of a protogalactic gas cloud (Buder et al. 2022; Efstathiou and Jones 1980; Nissen and Schuster 2010).

In the field of spectroscopy, chemical signatures of stars are usually acquired with one of two most common methods: the equivalent width method and the synthetic spectral fitting (Aufdenberg 2003; Blanco-Cuaresma et al. 2014a). The equivalent width method is tied to the physical concept of the 'curve of growth', whereas the synthetic spectral fitting technique makes a full synthesis of a spectrum and is more regularly utilized nowadays. Both methods will be described in Chapter 3 of this thesis.

Nissen and Schuster 2010 analyzed 94 dwarf stars in the solar neighborhood with effective temperatures of $5200 < T_{\rm eff} < 6300$ K and metallicities of $-1.6 <$ [Fe/H] < -0.4. Sixteen of this sample exhibit thick-disk kinematics whereas the others demonstrate halo kinematics in that they have a total space velocity with respect to the local standard of rest larger than 180 km/s. Nissen & Schuster carried out a differential abundance analysis using the equivalent width method (assuming local thermodynamic equilibrium (LTE) and MARCS model atmospheres) showing that the Galactic halo consists of two stellar populations: "high-α" and "low-α" stars, where α refers to the average abundance of neutral magnesium, silicon, calcium and titanium. The differential abundance analysis was performed with respect to the two bright disk stars HD 22879 and HD 76932 (Nissen and Schuster 2010).

Nissen & Schuster argued in their series of papers that the low-α population is most likely accreted from satellite dwarf galaxies whereas the high-α population could belong to an "in-situ" inner halo population, or alternatively, consist of ancient disk or bulge stars that were kinematically "heated" due to mergers with dSphs; Schuster et al. 2012 have suggested a dual scenario of an "in-situ" inner halo population and kinematic "heating" due to accretion. Their conclusions were based on obtained differential abundances of the aforementioned α elements and Na `I`, Ni `I` Mn `I`, Cu `I`, Zn `I`, Ba `II` and Y `II` (Nissen and Schuster 2010; Nissen and Schuster 2011; Schuster et al. 2012). In confirmation, recent Gaia studies have shown that a merger of the so-called Gaia-Enceladus system could explain these two distinct halo populations (Helmi et al. 2018).

In this bachelor thesis, I study archival blue and red UVES absorption line spectra of CD-51 4628, which was one of the low-α halo stars previously studied by Nissen and Schuster 2010 over the red wavelength range of 480 - 680 nm. Coincidentally, CD-51 4628 is also included in a common set of calibration stars, dubbed the Gaia FGK Benchmark Stars, as HD 298986 (Blanco-Cuaresma et al. 2014a; Hawkins et al. 2016; Wenger et al. 2000). Thus, for the first time, the blue spectrum of CD-51 4628 will be analyzed in detail such that our total wavelength range corresponds to 329 - 665 nm. Therefore, our aim is to determine the differential abundances of s- and r-process elements (e.g., yttrium and europium), in addition to those elements measured by Nissen and Schuster 2010 and Nissen and Schuster 2011, by analyzing the blue and red high-resolution spectra of CD-51 4628 making use of the integrated spectroscopic software framework `iSpec` and compare our results to stars coming from dSphs in general terms (Blanco-Cuaresma 2019; Blanco-Cuaresma et al. 2014a). Table 1.1 presents our complete list of 'interesting' elements.

This thesis presents the galactic archaeology in relation to the Milky Way and the physics behind slow and rapid neutron-capture processes (i.e., s- and r-process) in Chapter 2. In Chapter 3,

Table 1.1: This table lists the chemical elements of interest for the abundance analysis with the blue and red spectra of CD-51 4628. The last row presents the elements which are 'new' compared to Nissen and Schuster 2010 and Nissen and Schuster 2011.

Chemical elements of interest				
Na I	Mg I	Si I	Ca I	Ti I
Fe I	Fe II	Ni I	Y II	Ba II
La II	Nd II	Eu II	Os I	Th II

a technical overview of spectroscopy, the equivalent width method and the synthetic spectral fitting technique will be covered. Then, in Chapter 4, a general introduction to `iSpec` will be followed by comprehensive descriptions of the processing of the raw data and the spectral analysis of CD-51 4628. In Chapter 5 and Chapter 6, the results obtained will be presented and further discussed by performing comparisons with analogous literature studies. Lastly, a summary of the conclusions can be found in Chapter 7.

Chapter 2

Astrophysical Background

In this chapter, the relevant background to galactic archaeology in relation to the Milky Way and the physics behind slow and rapid neutron-capture processes are presented.

2.1 Galactic Archaeology

The existence of two distinct stellar populations in the Galactic halo could suggest different origins: some of the (low-α) halo stars were accreted from dwarf spheroidal satellite galaxies which might have merged with the Milky Way at an earlier time in its history (Deason et al. 2018; Helmi et al. 2018; Nissen and Schuster 2010). Particularly, a system dubbed Gaia-Enceladus (or occasionally overarchingly referred to as Gaia-Sausage-Enceladus) could have supplied the low-α population in the Galactic inner halo following an accretion process with the Milky Way (Buder et al. 2022; Matsuno et al. 2019; Nissen and Schuster 2011). This merger scenario is supported by comparable chemical signatures and retrograde kinematics between Gaia-Enceladus regions and the low-α stellar population (Helmi et al. 2018; Matsuno et al. 2019; Nissen and Schuster 2010). The idea that the Galactic halo is composed of infalling fragments of extragalactic stellar populations has been made already by Searle and Zinn 1978. Nowadays, the hierarchical galaxy formation scenario is supported by studies such as Schlaufman et al. 2009, which present evidence for halo substructures due to previous mergers with stellar systems.

For what concerns chemical signatures, it should be noted that this area of Galactic archaeology exploits the astronomical postulate that stellar atmospheres typically retain chemical information regarding the surrounding interstellar medium in which the star was formed (Burbidge et al. 1957). However, the orbital parameters that define dynamical components such as the halo and the thick-disk kinematics are liable to evolve over a certain time period, which would imply that separate stellar populations might eventually start to overlap (Buder et al. 2022). Thus, elemental abundance analyses can provide more stringent differentiations between various stellar populations based on their absorption line spectra. As an example, the kinematic overlap between the metallicities and α-enhancement of stars from the Galactic thin-disk, thick-disk and halo is depicted in Figure 2.1, which is adapted from Venn et al. 2004. Figure 2.1a and Figure 2.1b show the trends of the metallicity [Fe/H] and the α-enhancement [α/Fe] for the Galactic components. For instance, the thin disk is categorized by a narrow range in metallicities at a near constant rotation velocity of approximately 200 km/s and large spread of [α/Fe] at this velocity. The Galactic halo comprises a wider range of metallicities ([Fe/H] $\sim$ -2.5 $-$ -0.5) and α-enhancements ([α/Fe] $\sim 0 - 0.5$) correlated with a broader range of rotation velocities ($V \sim$ -150 $-$ 150 km/s).

Consequently, it is of significant importance to study the Galactic stellar halo and its intrinsic structure by means of chemical abundance analyses (in combination with kinematics) in order to thoroughly understand the formation and evolution of the Milky Way, even though its mass accounts for merely 1% of the Galaxy's total stellar mass (Bland-Hawthorn and Gerhard 2016). Therefore, by studying the absorption line spectra of a low-α halo star, it becomes possible to catch a glimpse of the fossilized chemical signature from its extragalactic birth site: a dwarf

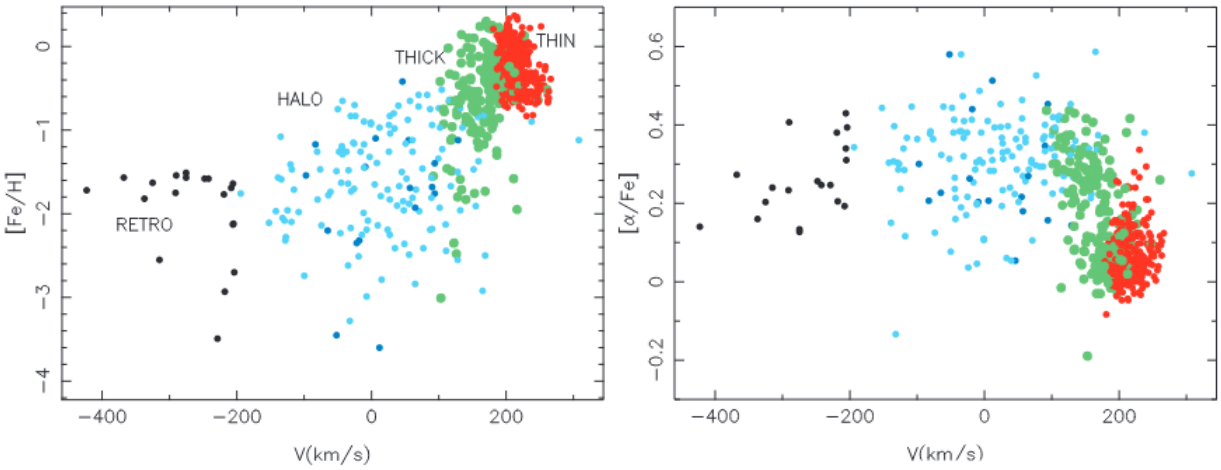

Figure 2.1: (a) Plot of the measurements of metallicity [Fe/H] on the y-axis and the rotation velocity V in the plane of the Milky Way in km/s on the x-axis and (b) plot of the measurements of α-enhancement [α/Fe] on the y-axis and the rotation velocity V in km/s on the x-axis. Stars from the following Galactic components are included: thin-disk (red), thick-disk (green) and halo (cyan). Black and blue dots respectively indicate stars with an extreme retrograde component and a high-velocity Toomre component (i.e., $T = (U^2 + W^2)^{1/2} > 340$ km/s, where U and W represent two of the three components comprising an object's Galactic space velocity). These plots come from Venn et al. 2004.

galaxy that subsequently merged with the Milky Way (Nissen and Schuster 2010). As an F-type star and one of the Gaia FGK Benchmark Stars, CD-51 4628 is an ideal candidate for obtaining a reliable fossil record from its chemical abundances (Jofré et al. 2019; LeBlanc 2010).

2.2 Slow and Rapid Neutron-Capture Processes

In order to comprehend the significance of observing s- and r-process elements in stellar spectra, we first need to understand where these elements originate from. For elements up to the iron-peak ($21 \leq Z \leq 30$), the principal production process is nuclear fusion in the stellar core after which the elements are released in supernova explosions and carried away by stellar winds into the interstellar medium (LeBlanc 2010; Maciel 2015; Sneden et al. 2008). Specifically, lighter elements with $Z \leq 13$ can be produced as a by-product during hydrogen fusion reactions and they belong to a group dubbed proton-capture elements. The α elements comprise elements with even atomic numbers and whose main isotopes contain multiples of the stable He-4 nucleus, e.g. O, Mg, Si, S, Ca and Ti (Sneden et al. 2008). It should be noted that elements can belong to more than one of these groups simultaneously.

As stated in Nissen and Schuster 2010 and LeBlanc 2010, the abundances of α elements (and iron) are typically supplied by Type-II supernovae (SNe II), an explosion of a massive star with a stellar mass of $M_* \geq 10 M_\odot$ on a timescale of $\sim 10^7$ years. Iron can also be produced in Type-Ia supernovae (SNe Ia), whose progenitor is a white dwarf star accreting mass from a companion star in a binary system, on a longer timescale of $\sim 10^9$ years (LeBlanc 2010; Nissen and Schuster 2010). Therefore, a (high mass) system with a fast chemical evolution (i.e., a high star formation rate) would be enriched by SNe II up to a relative high [Fe/H] leading to a high-α stellar population at a given [Fe/H], whereas a slower chemical evolution from a lower mass galaxy could

be enriched by SNe Ia at a particular [Fe/H] which creates a 'knee' going to lower α-abundances when plotting [α/Fe] against [Fe/H] of galactic stars (Hendricks et al. 2014; Nissen and Schuster 2010). Depending on the mass of the galaxy, this 'knee' is believed to shift to lower [Fe/H] for a low-mass galaxy (e.g., dSphs) due to its lower efficiency star formation history (resulting in SNe Ia enriching the interstellar medium) and to higher [Fe/H] in a high-mass galaxy (e.g., the Milky Way) (Hendricks et al. 2014; Walcher et al. 2015).

The neutron-capture elements ($Z > 30$) are produced, as the name would suggest, by neutron-capture processes of which there are two major ones: the slow neutron-capture process (s-process) and the rapid neutron-capture process (r-process) (LeBlanc 2010; Sneden et al. 2008). After an atomic nucleus captures a neutron (or multiple neutrons) and the nucleus becomes unstable due to a neutron excess, a neutron might be converted to a proton through a β^- decay,

$$n \rightarrow p + e^- + \overline{\nu_e} \tag{2.1}$$

such that the atomic number of the nucleus increases to $Z + 1$ (LeBlanc 2010). If a β^- decay occurs before the nucleus captures another neutron, we are speaking of a slow neutron-capture process (LeBlanc 2010; Sneden et al. 2008). Otherwise, if neutrons pile onto the nucleus and do not have enough time to decay to protons between captures, the neutron-capture process is categorized as rapid and stable r-process elements are created following the eventual decay of the excess neutrons, when the half-life of the unstable isotope becomes shorter than the neutron-capture time (LeBlanc 2010; Sneden et al. 2008). It should be noted that the r-process can create elements heavier than ^{209}Bi whereas the s-process cannot due to ^{209}Bi entering a gridlock of decay and neutron-capture reactions, as described in LeBlanc 2010. Adopted from LeBlanc 2010, Figure 2.2 provides a visual representation of r- and s-processes. In this figure, the letter p indicates a p-process element which is formed by certain p-process reactions with proton-rich isotopes; for further elaboration see Section 6.12.2 in LeBlanc 2010.

Additionally, the s-process can be divided into main, strong and weak channels (Hansen et al. 2014; Sneden et al. 2008; Van der Swaelmen et al. 2016). In particular, the weak s-process predominantly accounts for elements with an atomic mass $A = Z + N \leq 90$ and is linked to helium core and carbon shell burning in massive fast-rotating stars, whereas the main and strong channels contribute to elements with $A \sim 90 - 208$ and are connected to asymptotic giant branch (AGB) stars (Hansen et al. 2014; LeBlanc 2010; Van der Swaelmen et al. 2016). There are three s-process "peaks" which are located near the so-called neutron magic nuclei with $N = 50$, 82 and 126 for which atomic nuclei are extremely stable (Martinou and Bonatsos 2019; Sneden et al. 2008). Near these numbers, the (neutron-)capture cross section decreases in accordance with the increase in the produced s-process abundances (Sneden et al. 2008). Hence, a distinction is made between light s-process elements (first peak; e.g., Sr and Y), heavy s-process elements (second peak; e.g., Ba, La and Nd) and third-peak elements near Pb and Bi.

The r-process creates elements with $50 < A < 130$ and $A > 130$ in the dynamic ejecta of neutron star mergers, as suggested by Rosswog et al. 2014. Alternatively, the r-process could be associated with neutrino-driven winds from core-collapse supernovae and electron-capture supernovae resulting from the collapse of O-Ne-Mg cores (Arcones and Montes 2011; Wanajo et al. 2011). Nonetheless, it should be noted that these scenarios are mainly hypothetical and a consensus is not yet reached on definite r-process sites, except there is likely more than one (Van der Swaelmen et al. 2016). Since the heavy elements with $Z > 30$ have their strongest transitions mostly in the blue, studying blue stellar spectra will provide clues regarding the s-

and r-process sites and/or enrichment in stellar systems (Hansen 2022).

On that account, we have shown why studying (blue) stellar spectra would be of great interest for understanding the formation history of the Milky Way or any other galaxy via the fossilized chemical signatures found in halo stars.

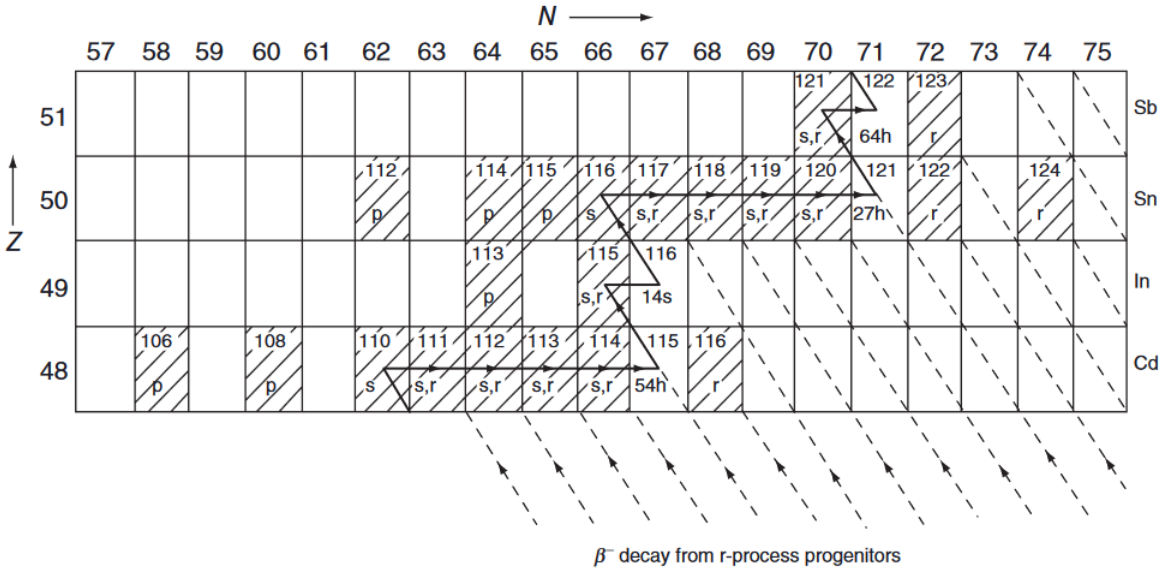

Figure 2.2: Schematic drawing of the nucleosynthesis of cadmium (Cd) to antimony (Sb) via the s-process (solid line), with the atomic number Z on the supposed y-axis and the neutron number N on the x-axis. The letters p, r and s indicate whether an element is produced by the p-, r- and/or s-process. The indicated times in hours and seconds represent approximate half-lifes of unstable isotopes. This figure comes from LeBlanc 2010.

Chapter 3

Spectroscopy

During the early 1800s, Kirchoff established the groundwork for stellar spectroscopy by describing the three types of stellar spectra which can exist: continuous, emission and absorption (Robinson 2007). For example, plasma comprising a stellar core would produce a continuous spectrum indicative of a (near) black body (Tennyson 2019). Emission lines are produced by hot low-density gasses spontaneously emitting photons at discrete wavelengths (Robinson 2007; Tennyson 2019). Absorption lines are due to the presence of atoms (and sometimes molecules) in the cooler photosphere of a star, where flux 'depressions' in the continuum represent specific atomic energy transitions at those wavelengths (Robinson 2007; Tennyson 2019). Since transitions between atomic energy levels require distinct photon energies (i.e., photons with a certain wavelength), it is possible to ascertain which atomic species are present in the star's outer layer. There are two common methods with which chemical abundances can be determined from stellar spectra: the equivalent width method and the synthetic spectral fitting technique, for which the subsequent sections provide further elaboration (Aufdenberg 2003; Blanco-Cuaresma et al. 2014a).

Modern spectrographs provide spectra by splitting and focusing the incoming light with prisms, gratings and mirrors onto a CCD detector (Hearnshaw 2009). Naturally, the experimental set-up influences the resolving power of the spectrograph. For high resolution spectrographs, there are two common types of arrangements which can achieve high resolving power: coudé and échelle (Hearnshaw 2009). In this thesis, only the echelle arrangement will be considered which utilizes échelle gratings with a high blaze angle ($> 45^{\circ}$). A blazed grating, consisting of angled grooves with an asymmetric V-shape, was found to be more efficient than ordinary diffraction gratings by Wood in 1910 and produces a high resolving power in an échelle arrangement (Hearnshaw 2009). Spectral lines can be more easily identified and separated in high resolution spectra than in low resolution spectra (as expected), but the star needs to be relatively bright as splitting light into many more resolution elements requires a lot of photons to work well, especially in the highest resolution spectra.

Adjacent spectral lines can remain blended with each other such that they can barely be distinguished. Particularly, the damping wings of strong hydrogen absorption lines are frequently blended (Maciel 2015; Robinson 2007). Furthermore, the dominant presence of hydrogen gives rise to the Balmer and Paschen jumps, spectral features which can be complicated to model and where chemical abundances can be challenging to ascertain, since the continuum level is difficult to determine (Robinson 2007; Tennyson 2019). The Balmer jump occurs around 364.7 nm and the Paschen jump around 821.2 nm, at which photon energies can ionize hydrogen atoms from the principal levels $n = 2$ and $n = 3$ respectively. Since high-energy photons with wavelengths shorter than 364.7 nm can ionize hydrogen atoms from $n = 2$, the continuum usually significantly drops on the blue side of the Balmer jump in stars with strong hydrogen line intensities (LeBlanc 2010; Robinson 2007; Tennyson 2019).

3.1 Equivalent Width Method

The equivalent width method is one of the standard methods used to determine the abundances of chemical elements (Aufdenberg 2003). Schematically, the (line) equivalent width W_λ is frequently defined in accordance with figures akin to Figure 3.1 (LeBlanc 2010; Maciel 2015; Robinson 2007). Physically, the equivalent width of a spectral line is defined as the width of a hypothetical rectangular spectral line which 'holds' the same amount of total energy that is absorbed in the original spectral line (LeBlanc 2010; Maciel 2015). In order to ascertain chemical abundances from stellar spectra using equivalent widths, a relationship between the equivalent width W_λ and the atomic abundance N_j of a lower energy level j is necessary: the curve of growth (Aufdenberg 2003; LeBlanc 2010; Maciel 2015).

As presented in Figure 3.2, the curve of growth is divided into three sections depicting the linear, saturated and square root part of the curve (Maciel 2015). For the linear part of the curve of growth we can write,

$$\frac{W_\lambda}{\lambda_{jk}} = \frac{\pi e^2}{m_e c^2} N_j f_{jk} \lambda_{jk} \tag{3.1}$$

where λ_{jk} represents the wavelength of the absorbed photon exciting an electron in an atom from a lower energy level j to a higher energy level k, f_{jk} the oscillator strength for this transition, c the speed of light, m_e the mass of an electron and e the charge of an electron (Maciel 2015). Equation 2.1 is valid for weak lines for which the optical depth[1] $\tau_\nu << 1$. For the saturated part we have,

$$\frac{W_\lambda}{\lambda_{jk}} = \frac{2bF(\tau_0)}{c} \tag{3.2}$$

where b and $F(\tau_0)$ are given by,

$$b = \left(\frac{2kT}{m}\right)^{1/2} \tag{3.3}$$

$$F(\tau_0) = \int_0^\infty \left[1 - \exp\left(-\tau_0 e^{-x^2}\right)\right] dx \tag{3.4}$$

in which k represents the Boltzmann constant, T the temperature of the medium and m the mass of the absorbing atom when assuming a Doppler line profile (Maciel 2015). A Doppler line profile is produced by the thermal motions of the absorbing atoms broadening the spectral line (Maciel 2015; Robinson 2007). For the square root part we can write,

$$\frac{W_\lambda}{\lambda_{jk}} = \frac{2\pi e^2}{m_e c^2} f_{jk} \left[2\frac{g_j}{g_k} N_j\right]^{1/2} \tag{3.5}$$

where g_j and g_k represent the statistical weights of the lower and upper energy levels (Maciel 2015). With these equations, the total abundance of a chemical element can be determined when knowing the equivalent width of the spectral line and the intrinsic parameters of the energy transition $j \to k$.

[1]The optical depth τ_ν can be defined as the degree of opaqueness of a medium at a certain frequency ν, being equal to zero at the surface of a star (LeBlanc 2010).

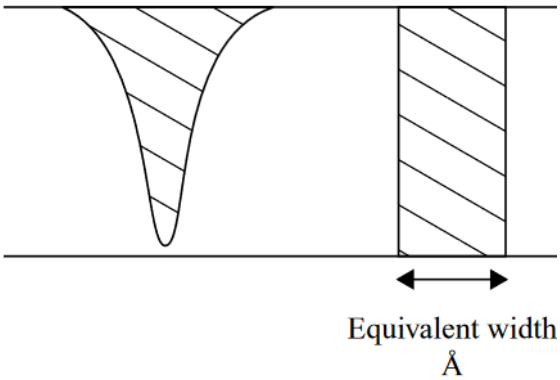

Figure 3.1: This figure depicts the schematic definition of the equivalent width W_λ, with the wavelength λ in units of Angström on the horizontal axis. Note that the shaded areas of the absorption line and the rectangle are meant to be equal. This figure has been adapted from Robinson 2007.

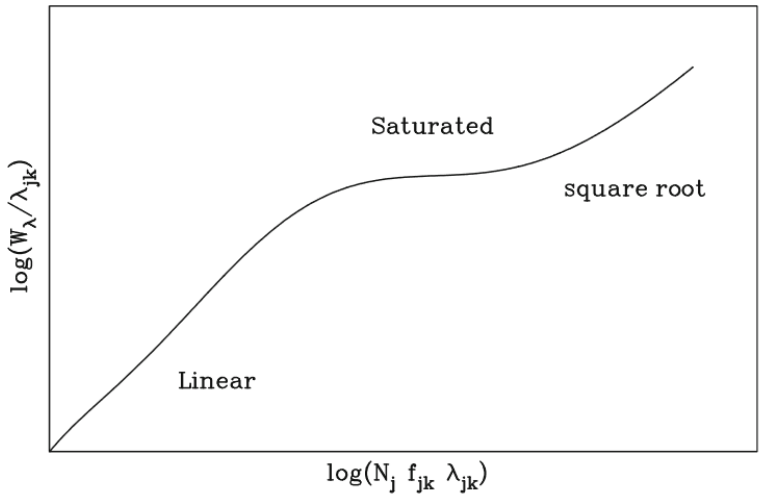

Figure 3.2: Schematic overview of the curve of growth with the reduced equivalent width $\log(W_\lambda/\lambda_{jk})$ on the y-axis and $\log(N_j f_{jk} \lambda_{jk})$ on the x-axis. Note that λ_{jk} represents the wavelength of the absorbed photon exciting an electron in an atom from a lower energy level j to a higher energy level k and f_{jk} the oscillator strength for this transition. This figure comes Maciel 2015.

3.2 Synthetic Spectral Fitting Technique

Compared to the equivalent width method, the synthetic spectral fitting technique is more contemporary (Aufdenberg 2003; Blanco-Cuaresma 2019). Nonetheless, the fundamental idea is relatively simple: by generating model stellar spectra over a broad span of atmospheric parameters (e.g., effective temperature, surface gravity, etc.) and chemical abundances with a synthesis code, comparisons with the observed stellar spectrum should yield the best estimated parameters and abundances (Gray and Corbally 1994). Synthesizing stellar absorption line spectra in a reliable way requires accurate models of stellar atmospheres such that a grid of pre-computed spectra can be created to which observed spectra can be compared (Blanco-Cuaresma 2019). The spectroscopic framework `iSpec` supports two of the most common model atmospheres, which are MARCS and ATLAS9 (Gustafsson et al. 2008; Kurucz 2005). Regarding the MARCS model atmospheres, Blanco-Cuaresma 2019 states that their pre-computed grids are generated with the solar abundances from Grevesse et al. 2007.

Then, radiative transfer codes are used to ascertain chemical abundances from stellar spectra when provided with a grid of pre-computed spectra and a set of (initial) atmospheric parameters (Blanco-Cuaresma 2019). Since most radiative transfer codes do not support spherical model atmospheres due to their complexity, grids computed with the plane-parallel approximation are utilized, which assumes that a stellar atmosphere consists of plane-parallel gas layers (infinite in the x- and y-directions and semi-infinite the negative z-direction, e.g. LeBlanc 2010). Additionally, all radiative transfer codes used in this thesis assume local thermodynamic equilibrium (LTE), which is a decent approximation for AFGKM stars, considering our scientific goals (Blanco-Cuaresma 2019).

Chapter 4

Methodology

In this chapter, a basic description of the VLT/UVES instrument will be given and a general introduction to the software framework `iSpec` (Blanco-Cuaresma 2019; Blanco-Cuaresma et al. 2014a) with which the processing of the raw data and the spectral analysis of CD-51 4628, which includes determining its atmospheric parameters from the red spectra and its (differential) chemical abundances, are carried out.

4.1 UVES

The Ultraviolet and Visual Echelle Spectrograph (UVES) is a high-resolution spectrograph located at the Very Large Telescope (VLT) facility in Chile, which is operated by the European Southern Observatory (ESO). The instrument consists of two 'arms' over which the incoming light can be divided, the UV-Blue and Visual-Red arms, such that their combined wavelength range could cover ∼300 - 1100 nm (Dekker et al. 2000). The broad wavelength coverage is achieved with a dichroic, which sends light to the UV-Blue and Visual-Red arms simultaneously[1]. As indicated by the spectograph's name, the instrument has an echelle setup accompanied by a blazed grating with a high blaze angle of approximately 76°.

Regarding our blue spectra, the setting with a central wavelength at 390 nm was utilized such that the minimum and maximum wavelengths correspond to 326 nm and 454 nm. The setting with a central wavelength at 564 nm was used on the red arm, yielding a wavelength range of 458 - 665 nm. However, a mosaic of two CCD chips is implemented in the red arm such that the CCD detector has a gap of about 0.96 mm in which there are no pixels to detect the incoming photons. Consequently, there are two distinct red spectra (i.e., one for each chip) which are separated by a gap of approximately 4.6 nm. In Table 4.1, the wavelength ranges and the observation dates and timestamps of our individual spectra are listed.

The spectra were observed one after the other in good seeing conditions[2] and taken from the ESO Archive and processed by the ESO UVES pipeline (Freudling et al. 2013). The exposure time of each spectrum is approximately 1200 seconds and the spectral resolution is R $\sim$ 55000 for the blue and red spectra. The signal-to-noise ratio of the individual spectra will be estimated with `iSpec` in Section 4.3.

[1] UV-Visual Echelle Spectrograph User manual: https://www.eso.org/sci/facilities/paranal/instruments/uves/doc/ESO_411892_User_Manual_P110.pdf

[2] In the ESO archive for raw data, the FWHM seeing value at the start of the observations is listed as 0.85".

Table 4.1: Wavelength ranges and observation specifics of the individual spectra.

Spectrum	Wavelength range [nm]	Observation Timestamp	Date
390i	326 - 454	02:51:46.925	2001-03-08
390ii	326 - 454	03:12:34.395	2001-03-08
390iii	326 - 454	03:33:20.958	2001-03-08
564li	458 - 562	02:51:40.819	2001-03-08
564lii	458 - 562	03:12:39.855	2001-03-08
564liii	458 - 562	03:33:34.105	2001-03-08
564ui	567 - 665	02:51:40.819	2001-03-08
564uii	567 - 665	03:12:39.855	2001-03-08
564uiii	567 - 665	03:33:34.105	2001-03-08

4.2 `iSpec`

The spectral analysis is carried out with the integrated spectroscopic software framework `iSpec` (Blanco-Cuaresma 2019; Blanco-Cuaresma et al. 2014a). Blanco-Cuaresma et al. 2014b utilized `iSpec` to build the Gaia FGK Benchmark Stars library from high-resolution spectra provided by the Gaia-ESO Public Spectroscopic Survey (GES, Gilmore et al. 2012; Randich et al. 2013), in which CD-51 4628 is labeled as HD 298986 (Hawkins et al. 2016; Wenger et al. 2000). Particularly, `iSpec` is designed to ascertain atmospheric parameters and individual chemical abundances of AFGKM stars from their absorption line spectra using the equivalent width method and the synthetic spectral fitting technique (Blanco-Cuaresma 2019). With respect to the synthetic spectral fitting technique, the code works practically the same as the description in Section 3.2; an implemented nonlinear least-squares fitting algorithm is utilized to find the smallest difference between the observed spectrum and an interpolated synthetic spectrum from a pre-computed grid during an iterative process (Blanco-Cuaresma 2019; Blanco-Cuaresma et al. 2014a). Regarding the equivalent width method, Gaussian models are fitted to the indicated spectral lines such that an equivalent width can be determined from their integrated area.

The results are returned to the user either through the visual interface of `iSpec` or as the output from a Python script which utilizes functions from `iSpec`. For instance, a Python script allows for the opportunity to manually generate synthetic spectra with input atmospheric parameters and specific chemical abundances (e.g., for creating a new archive of pre-computed grids), whereas the interface's options are restricted to fixing only the atmospheric parameters. Given the limited timeframe of this thesis, the spectral analysis was primarily performed via the user-friendly visual interface. Hence, throughout this work all aspects of the spectral analysis are carried out in the framework of `iSpec` and the advice given in Blanco-Cuaresma 2019, Blanco-Cuaresma et al. 2014a and `iSpec`'s manual[3].

[3]Available via https://www.blancocuaresma.com/s/iSpec/manual/introduction

4.3 Raw Data Processing

As presented in Table 4.1, we have three sets of three spectra from the ESO Archive for raw data. The files with the flux calibrated data and their corresponding errors were initially separated, and manually combined with a short Python script using functions from the module NumPy (Van der Walt et al. 2011). As an example, Figure 4.1 presents the three spectra 564li-iii. On the far left-hand side of the plot, a region can be seen which cannot be utilized for the spectral analysis, most likely due to an instrumental effect that cannot be corrected.

`iSpec` can gauge the spectra's signal-to-noise ratio (SNR) from the flux errors by dividing the fluxes by the error array. In Table 4.2, the SNRs of each spectrum can be found. Averaging the sets of spectra yields three mean spectra with which the spectral analysis will be carried out. Subsequently, the flux errors are required to be properly propagated as well. As described in Klein-Douwel 2019, the general formula for error propagation can be written as,

$$\Delta Q = \sqrt{\left(\frac{\delta f}{\delta x}\Delta x\right)^2 + \left(\frac{\delta f}{\delta y}\Delta y\right)^2 + \left(\frac{\delta f}{\delta z}\Delta z\right)^2 + ...} \tag{4.1}$$

in which,

$$Q = f(x, y, z, ...) \tag{4.2}$$

is any general function. Consequently, we can write the error in the averaged fluxes in the following way:

$$\Delta F_{mean} = \frac{1}{3}\sqrt{(\Delta F_i)^2 + (\Delta F_{ii})^2 + (\Delta F_{iii})^2} \tag{4.3}$$

where ΔF_{mean} represents the flux errors of the averaged fluxes and ΔF_{i-iii} the flux errors of the three individual spectra which are averaged. Additionally, all spectra are aligned within their respective sets during the combining, after checking that the positions of spectral line masks coincide within the sets. Figure 4.2 shows the entire range of wavelengths covered with the final three spectra, in which the Balmer jump can be observed around 365 nm. Due to the gaps between the spectra, the wavelength regions which can be used correspond to 330 - 451 nm (`Blue`), 462 - 559 nm (`RedL`) and 569 - 665 nm (`RedU`). As a result of the error propagation, the estimated SNRs of `Blue`, `RedL` and `RedU` have increased to 286, 540 and 561 compared to the original spectra's SNRs, by approximately a factor of $\sqrt{3}$ on average.

Before being able to use the averaged spectra for determining the stellar atmospheric parameters and the abundance analysis, we need to normalize the spectra by fitting a model function to the continuum and dividing by the fitted continuum, i.e. the continuum should be along a horizontal line corresponding to a flux of 1. First, the 'corrupted' region in `RedL` is removed by cropping the spectrum to 462.5 nm. The continuum can only be properly fitted if the spectra are barycentric and radial velocity corrected such that their wavelengths match the rest wavelengths of atomic energy transitions. The barycentric velocity in `iSpec` is the velocity due to the Earth orbiting around its own axis *and* around the center of mass of our solar system (the heliocentric velocity), since the telescope on Earth is also moving with a certain velocity with respect to the observed star (Stumpff 1980; Wright and Kanodia 2020).

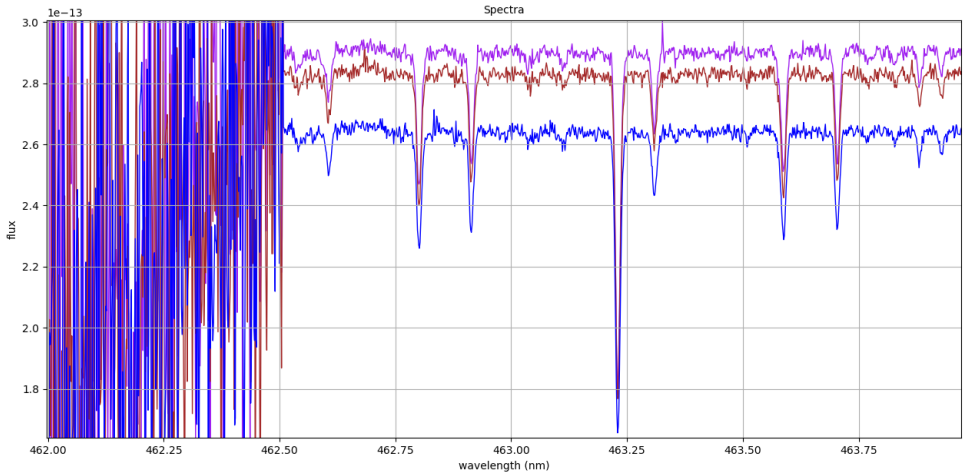

Figure 4.1: Magnified plot of 564li (blue), 564lii (red) and 564liii (purple) with the flux in ergs s^{-1} cm^{-2} $\mathring{A}^{-1}$ on the y-axis and the wavelength in nanometers on the x-axis. This plot is made with `iSpec`.

Table 4.2: Signal-to-noise ratios of the individual spectra, estimated from the flux errors with `iSpec`.

Spectrum	390i	390ii	390iii	564li	564lii	564liii	564ui	564uii	564uiii
SNR	163.24	165.48	166.51	305.67	313.48	315.78	317.92	325.93	328.55

Subtracting the barycentric velocity gives the star's radial velocity, which is the velocity with respect to the Solar System's barycenter (Wright and Kanodia 2020). Therefore, the observed wavelengths will be shifted according to the relativistic Doppler shift formula,

$$\lambda_{corrected} = \lambda_{observed}\sqrt{\frac{1-\frac{v_r}{c}}{1+\frac{v_r}{c}}} \tag{4.4}$$

where v_r is the radial velocity in km/s (Robinson 2007). `iSpec` can determine the barycentric and radial velocity of a spectrum by comparing its atomic lines with a telluric line mask and an atomic line mask. Since the observed calibrated fluxes provided by the UVES pipeline were too small for `iSpec` to work with, the fluxes were all multiplied by a factor of 10^{13} making them lie largely above a flux of 1. In Table 4.3, the estimated barycentric and radial velocities of `Blue`, `RedL` and `RedU` can be found. The positive radial velocities indicate that CD-51 4628 is moving away from us, resulting in red-shifted spectral lines (Robinson 2007). Nonetheless, it should be noted that a barycentric velocity of -5.67 km/s is computed by `iSpec` when using the observation timestamp and CD-51 4628's coordinates in Right Ascension (RA) and Declination (DEC) from 390i.

Now, the continuum can be fitted using one of the four models provided by `iSpec`: splines, polynomy, a pre-computed template spectrum or a fixed value fit. Due to the unconventional shapes of the spectra, the more flexible splines model was utilized for both the blue and red spectra. In Table 4.4, the parameters of the fits for the spectra are presented. The wavelength steps for median and max selection are related to the median and maximum filters which `iSpec`

applies to minimize the effects of noise and avoid (strong) absorption lines. Additionally, `iSpec` resamples the fitted continuum with a custom wavelength step, ascertained by dividing the minimum wavelength by the input resolution. Regarding `Blue`, we experimented with two continuum fits which use a slightly different wavelength step for max selection. As shown in Figure 4.3, the Balmer jump is challenging to accurately model with either Fit 1 or Fit 2. Since the two fits yield two distinct normalized spectra (which are dubbed `Blue 1` and `Blue 2`), the abundance analysis in the blue will be performed with both normalized spectra concomitantly.

When fitting the continuum, `iSpec` seems to interpolate the flux errors and subsequently decreases the SNRs of normalized spectra[4]. In order to reinstate the initial SNRs, a short Python script computes the median ratio between the fluxes and flux errors of a spectrum and multiplies the normalized fluxes by this median ratio to restore the errors of the normalized spectrum. After checking the SNRs of the normalized spectra, we have determined that the SNRs are in that case 'stable' between the original and normalized spectra.

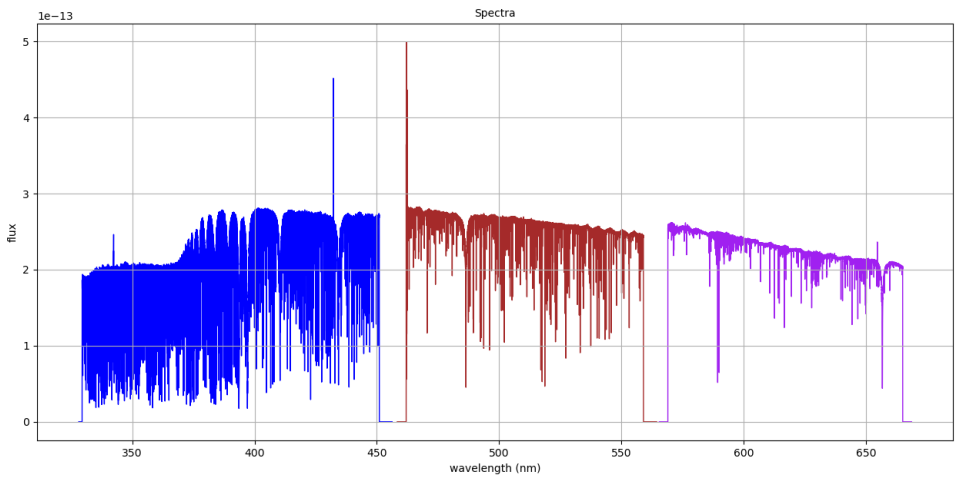

Figure 4.2: Plot of the three different wavelength ranges observed simultaneously with the flux in ergs s^{-1} cm^{-2} $Å^{-1}$ on the y-axis and the wavelength in nanometers on the x-axis. It should be noted that the spectra are not exactly on the same flux scale. For our convenience, the spectra will be referred to as `Blue` (blue), `RedL` (red) and `RedU` (purple) from hereon. This plot is made with `iSpec`.

Table 4.3: Barycentric and radial velocities of `Blue`, `RedL` and `RedU`, estimated by comparing their atomic lines with a telluric line mask and an atomic line mask with `iSpec`.

Spectrum	Barycentric velocity [km/s]	Radial velocity [km/s]
`Blue`	*	191.99 ± 0.10
`RedL`	-0.32 ± 0.28	192.19 ± 0.14
`RedU`	-0.25 ± 0.08	192.25 ± 0.26

*`iSpec` returned the following warning: "Not enough data for finding peaks and base points."

[4]See line 287 in the file continuum.py in the folder ispec, which is publicly available via https://github.com/marblestation/iSpec.

Table 4.4: Model parameters of the fitted continuum for `Blue`, `RedL` and `RedU`.

Model parameters	`Blue`	`RedL`	`RedU`
Number of splines	50	20	20
Degree	5	2	2
Resolution	55000	55000	55000
Filtering order	median+max	median+max	median+max
Wavelength step for median selection	0.05	0.05	0.05
Wavelength step for max selection	2.0 (Fit 1) 3.0 (Fit 2)	2.5	2.0
Weighted fitting[1]	x	x	x
Ignoring strong lines[2]	x	x	x
Strong line probability threshold	0.5	0.5	0.5

[1]Original label in `iSpec`: "Use spectrum's errors as weights for the fitting process"
[2]Original label in `iSpec`: "Automatically find and ignore strong lines"

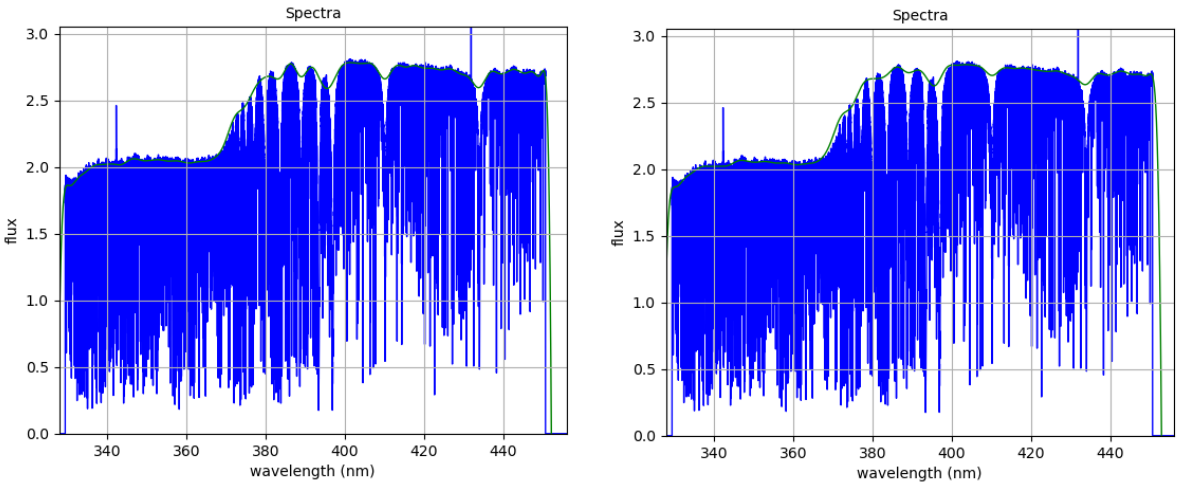

Figure 4.3: Plot of `Blue`'s continuum modeled by (a) Fit 1 and (b) Fit 2, with the flux in normalized units on the y-axis and the wavelength in nanometers on the x-axis. These plots are made with `iSpec`.

4.4 Determining Atmospheric Parameters

The atmospheric parameters of CD-51 4628 are determined with the normalized spectra of `RedL` and `RedU`, and compared to the literature values reported in Nissen and Schuster 2010 in Chapter 6. Particularly, the stellar atmospheric parameters consist of the effective temperature T_{eff}, the surface gravity $log(g)$, the metallicity [Fe/H], the α-enhancement [α/Fe] and the microturbulence velocity v_{mic}. As described in Blanco-Cuaresma et al. 2014a, we use the neutral and ionized iron lines to obtain these parameters by imposing excitation equilibrium and ionization balance. Excitation equilibrium implies that there should be no trends when the abundances of Fe `I` and Fe `II` are plotted against the line excitation potential 'lower state (eV)'; ionization balance means that the average Fe `I` abundance is equivalent to the average Fe `II` abundance. Furthermore, there should be no trends when the iron abundances are plotted against the reduced equivalent width. On a side note, the continuum of the normalized red spectra is fitted with the same parameters presented in Table 4.4.

iSpec can find the line masks of neutral and ionized iron lines when given the required minimum depth of the absorption lines with respect to the continuum (set to 0.05 or 5%), the maximum depth (set to 1.0 or 100%), the spectrum's resolution (set to 55000), the velocity with respect to the telluric lines in km/s (which is equal to the negative of the radial velocity) and a line list for cross-referencing the spectral lines with atomic line transitions. Line list version 6 from the GES line list is utilized, which was specifically designed for homogeneous abundance analyses of stellar spectra from the GES (Blanco-Cuaresma 2019; Heiter et al. 2015). This line list takes into account hyperfine splitting (HFS) and isotopic shifts (ISO) and covers a wavelength range of 420 - 920 nm. In RedL, iSpec found 233 Fe I lines and 18 Fe II lines; in RedU, there are 61 Fe I lines and 5 Fe II lines. Customarily, iSpec automatically fits the found lines with a Gaussian model. Otherwise, the lines can be fitted by using the option 'Operations → Fit lines' and inputting the resolution, the velocity with respect to the telluric lines [km/s], the line list and a maximum atomic wavelength difference between the observed and theoretical wavelength peak of a line.

The equivalent width method is used to ascertain CD-51 4628's atmospheric parameters with the radiative transfer code MOOG EW, the MARCS model atmosphere MARCS.GES and the solar abundance table Asplund.2009. Regarding the choice of radiative transfer code, Blanco-Cuaresma et al. 2014a concluded that MOOG EW performs better than WIDTH9. Even though iSpec's pre-computed MARCS grids are generated with the solar abundances provided by Grevesse et al. 2007, we have utilized the most recent solar abundance table from Asplund et al. 2009. Since iSpec appears to assign a standard α-enhancement to different metallicity ranges, the α-enhancement will be fixed to the literature value reported in Nissen and Schuster 2010 which is provided as $[\alpha/\mathrm{Fe}] = 0.22$. It should be noted that a nonlinear least-squares fitting algorithm aims to reduce the impact of outliers on the results, when systematically adjusting the parameter estimates during various iterations (set to a maximum of 10 in our analysis) such that ionization balance and excitation equilibrium are most adequately achieved.

4.5 Abundance Analysis

In this section, we will discuss the abundance analysis performed with the normalized red spectra and blue spectra, where the errors of the normalized fluxes have been reinstated in the same manner as described above with respect to the normalized red spectra. The chemical abundances of our 'interesting' elements will be determined with the equivalent width method and the synthetic spectral fitting technique. In Appendix A, the absorption lines that were utilized during the abundance analysis are listed.

4.5.1 Equivalent Width Method

iSpec can ascertain differential chemical abundances with the equivalent width method when given the radiative transfer code, the model atmosphere, the solar abundance table and the stellar atmospheric parameters. Regarding the equivalent width method, iSpec determines a mean and median chemical abundance when utilizing multiple spectral lines, and we will use the median abundances to minimize the effect of outliers in the data (Bakker and Gravemeijer 2006). The standard deviation of the sample serves as the uncertainty on the results, which cannot be determined when utilizing a single line. In the following sections, the abundance analysis carried out with the red and blue spectra will be separately discussed. They all share the input

parameters for the radiative transfer code (MOOG EW), the model atmosphere (MARCS.GES) and the solar abundances (Asplund.2009).

4.5.1.1 Red Spectra

In order to determine the chemical abundances of CD-51 4628 from the normalized red spectra, line masks of the following elements are required: Na I, Mg I, Si I, Ca I, Ti I, Ni I, Y II, Ba II, La II, Nd II, Eu II, Os I and Th II. Once again, the line list version 6 from the GES line list was used when finding the line masks with iSpec. Spectral lines of La II, Nd II, Eu II, Os I and Th II could not be detected in either of the red spectra, reducing the list of elements. Due to the gap between RedL and RedU, their normalized spectra are treated independently. As with the determination of the atmospheric parameters, the continuum of the spectra is fitted with the same parameters presented in Table 4.4. Regarding the input atmospheric parameters, the preferred values acquired with the method from Section 4.4 are used to gauge the different effects of the equivalent width method and the synthetic spectral fitting technique on the results, and can be found in Table 5.1 in Chapter 5.

When determining the chemical abundances of the remaining elements, the lines identified by iSpec are cross-referenced with the line data reported in Table 3 of Nissen and Schuster 2011; only similar lines (i.e., wave peaks matching up to at least four digits) are utilized in the abundance analysis. Even so, each line from Nissen and Schuster 2011 will be checked and disregarded if it is poorly fitted by the Gaussian model or lies in a region which might be affected by telluric lines[5] and/or where absorption lines are badly blended or the continuum is poorly fitted. In RedL, this leaves us with 2 Ca I lines, 5 Ti I lines, 11 Ni I lines, 2 Y II lines; in RedU, we have 1 Mg I line, 1 Si I line, 3 Ca I lines and 2 Ba II lines. Unfortunately, no Na I lines were detected in RedL. In RedU, there was a single Na I line from Nissen and Schuster 2011 which could have been used, but it was located near the edge of the spectrum at 568.8 nm and the continuum was poorly fitted in this region during the normalization of RedU. Hence, this Na I line was not used.

4.5.1.2 Blue Spectra

Since the splines model did not manage to fit the continuum in the normalized blue spectra adequately, the continuum is simply fitted with a horizontal line at a fixed value of 1. Then, it is possible to find the line masks of our elements of interest (plus neutral and ionized iron) in Blue's normalized spectra with the VALD line list, which extends further into the blue than the GES line list and covers a wavelength range of 300 - 1100 nm. Whenever possible, the line masks are cross-referenced with the spectral lines reported in Hill et al. 2002 and poorly fitted or badly blended lines are disregarded. Examples of two badly blended and poorly fitted lines are shown in Figure 4.4, which depicts an Os I line and a Th II line. Otherwise, all line masks are utilized. Regarding Fit 1 and Fit 2, this leaves us with 1 Na I line, 14 Mg I lines, 2 Si I lines, 34-35 Ca I lines, 84-89 Ti I lines, 1175-1202 Fe I lines, 56-58 Fe II lines, 129-131 Ni II lines, 5 Y II lines, 1 Ba II line, 2 La II lines, 1 Nd II line, 1 Eu II line, zero Os I lines and zero Th II lines within the wavelength range.

As an experiment, the Balmer continuum will be treated as an independent section covering a wavelength range of 330 - 370 nm (Roederer et al. 2018a). For this region, there are generally

[5]Telluric lines are absorption lines from elements in Earth's atmosphere and need to be separated from the stellar absorption lines (Hadrava 2006).

no line lists reported in literature which we would be able to cross-reference with. Hence, we have 1 Na `I` line, 3 Mg `I` lines, zero Si `I` lines, 7-8 Ca `I` lines, 17-18 Ti `I` lines, 451-465 Fe `I` lines, 23-24 Fe `II` lines, 90 Ni `I` lines, 9 Y `II` lines, zero Ba `II` lines, 1 La `II` line, zero Nd `II` lines and zero Eu `II` lines. Regarding the abundance analysis, the atmospheric parameters reported in Nissen and Schuster 2010 are used since they comprise a complete set of parameters as opposed to utilizing a mixed set consisting of results from varying literature sources (which is not recommended by Blanco-Cuaresma 2019).

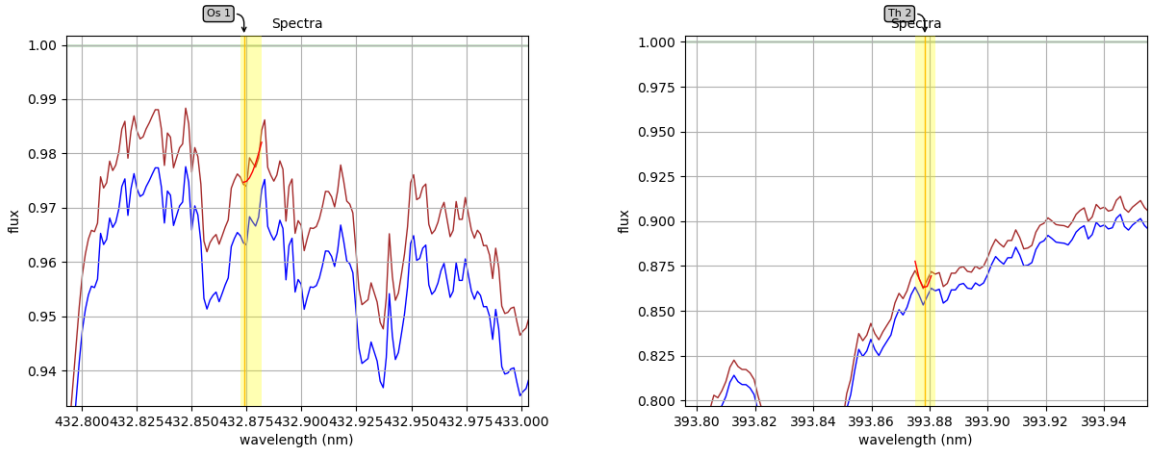

Figure 4.4: Plot of (a) an Os `I` line and (b) a Th `II` line at the same location in `Blue 1` (red) and `Blue 2` (blue), with the flux in normalized units on the y-axis and the wavelength in nanometers on the x-axis. The relatively short red lines in the yellow shaded regions follow the shape of the lines with a Gaussian model. These plots are made with `iSpec`.

4.5.2 Synthetic Spectral Fitting Technique

Comparatively to the equivalent width method, `iSpec` can determine differential chemical abundances with the synthetic spectral fitting technique when given the radiative transfer code, the model atmosphere, the solar abundance table, the line list, the stellar atmospheric parameters, the projected rotational velocity $V sin(i)$ [km/s], the macroturbulence velocity V_{mac} [km/s], the limb darkening coefficient and the radial velocity [km/s]. For the stellar atmospheric parameters, the results from Nissen and Schuster 2010 are utilized for both the blue and red spectra in all but two runs with `RedL` and `RedU`, as described above. Regarding the projected rotational velocity and the macroturbulence velocity, the values reported in the library of the Gaia FGK Benchmark Stars are used, even though this will yield a mixed set of parameters (Blanco-Cuaresma et al. 2014b). Hence, the following input parameters are used for all the runs in the abundance analysis: the radiative transfer code (`MOOG`), the model atmosphere (MARCS.GES), the solar abundances (Asplund.2009), the line list (VALD_300-1100nm), $V sin(i)$ (4.1 km/s), V_{mac} (7.88 km/s), the limb darkening coefficient (set to 0.6 as a rough approximation) and the (corrected) radial velocity (0 km/s). Additionally, we will re-use the spectral lines from the abundance analysis with the equivalent width method for these runs with the synthetic spectral fitting technique and set the maximum amount of iterations to 6.

Chapter 5

Results

Following the methodology described in the previous chapter, the determinations of CD-51 4628's atmospheric parameters and the results from the abundance analysis carried out with the (normalized) red and blue spectra will be presented in the subsequent sections.

5.1 Determining Atmospheric Parameters

We have determined the atmospheric parameters of CD-51 4628 from (the normalized spectra of) `RedU` and `RedL` separately, which can be found in Table 5.1. The second column presents the atmospheric parameters obtained from `RedU`, and the third column the initial atmospheric parameters obtained from `RedL`. Since their surface gravities appear to differ significantly and taking into consideration their relatively small uncertainties, we have fixed the surface gravity in the second run with `RedL` using the corresponding estimate from `RedU`, the results of which are shown in the fourth column of Table 5.1. Then, this set of parameters constitutes our preferred values for the atmospheric parameters of CD-51 4628, and this choice will be elaborated on in Chapter 6. However, as depicted in Figure 5.1b, the excitation potential slope of the second run displays a slight negative trend and is equal to -0.03 due to the fixing of the surface gravity. In Figure 5.1a, the excitation potential slope of the run with `RedU` is equal to 0.00 (i.e., no trends are found).

Table 5.1: Atmospheric parameters determined from `RedU` and `RedL` using the equivalent width method on the spectra's neutral and ionized iron lines. The 'NS10' column represents the atmospheric parameters of CD-51 4628 from Nissen and Schuster 2010.

Atmospheric parameters	`RedU`	`RedL`		NS10
T_{eff} [K]	6363.14 ± 91.58	6097.85 ± 91.14	6278.56 ± 23.31	6153 ± 30
$log(g)$	4.13 ± 0.13	3.82 ± 0.13	4.13*	4.31 ± 0.05
[Fe/H] [dex]	-1.26 ± 0.12	-1.48 ± 0.22	-1.36 ± 0.21	-1.30 ± 0.04
[α/Fe] [dex]	0.22*	0.22*	0.22*	0.22 ± 0.02
v_{mic} [km/s]	1.40 ± 0.09	1.53 ± 0.03	1.46 ± 0.04	1.4

*Fixed parameter

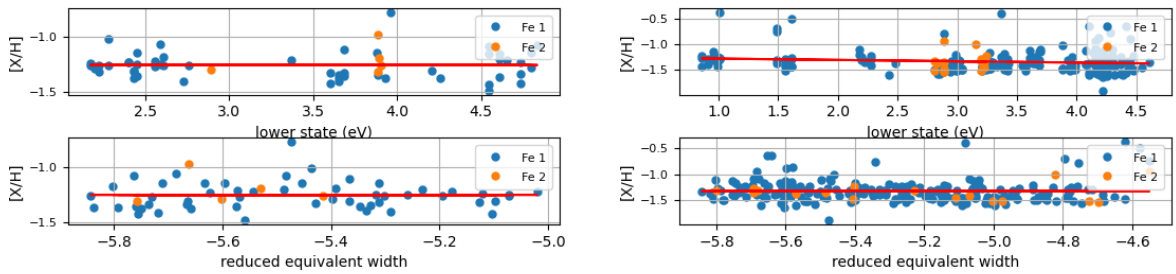

Figure 5.1: Plots of the variation in Fe `I` (blue dots) and Fe `II` (orange dots) abundances obtained from (a) `RedU` and (b) `RedL` (second run). [Fe `I`/H] and [Fe `II`/H] are plotted on the y-axis. The line excitation potential 'lower state (eV)' in electron volts is plotted on the upper x-axis and the reduced equivalent width on the lower x-axis. These plots are made with `iSpec`.

5.2 Abundance Analysis

5.2.1 Red Spectra

In Table 5.2, the results from the abundance analysis with `RedL` are presented. These chemical abundances were obtained using the equivalent width method with the preferred values of CD-51 4628's atmospheric parameters; the synthetic spectral fitting technique was also utilized with the preferred values of the stellar atmospheric parameters and the parameters from Nissen and Schuster 2010. Analogously, Table 5.3 shows the results obtained with `RedU`.

5.2.2 Blue Spectra

In Table 5.4, the results from the abundance analysis with the two normalized spectra of `Blue` are presented. These chemical abundances were obtained using the equivalent width method and the synthetic spectral fitting technique with the stellar atmospheric parameters from Nissen and Schuster 2010. Analogously, Table 5.5 shows the results obtained from `Blue 1` and `Blue 2` when merely considering the Balmer continuum region in these spectra (∼330 - 370 nm). Whenever available, chemical abundances from literature will be reported in the last columns of Table 5.4 and Table 5.5.

Table 5.2: Chemical abundances estimated from `RedL` using the equivalent width method and the synthetic spectral fitting technique on the corresponding spectral lines reported in Appendix A. Synthesis was performed with the preferred values of the atmospheric parameters and the results reported in Nissen and Schuster 2010. The 'Literature' column represents the chemical abundances of CD-51 4628 from Nissen and Schuster 2010 ([1]) and Nissen and Schuster 2011 ([2]).

Chemical	Equivalent widths	Synthesis		Literature
abundances [dex]	(ours)	(ours)	(NS10)	
[Ca `I`/Fe]	0.25 ± 0.03	0.37 ± 0.08	0.26 ± 0.08	0.31 ± 0.02 [1]
[Ti `I`/Fe]	0.24 ± 0.02	0.35 ± 0.05	0.19 ± 0.05	0.24 ± 0.02 [1]
[Ni `I`/Fe]	-0.13 ± 0.09	-0.04 ± 0.04	-0.15 ± 0.04	-0.10 ± 0.01 [1]
[Y `II`/Fe]	-0.17 ± 0.07	-0.07 ± 0.13	-0.10 ± 0.13	-0.11 ± 0.04 [2]

Table 5.3: Chemical abundances estimated from `RedU` using the equivalent width method and the synthetic spectral fitting technique on the corresponding spectral lines reported in Appendix A. Synthesis was performed with the preferred values of the atmospheric parameters and the results reported in Nissen and Schuster 2010. The 'Literature' column represents the chemical abundances of CD-51 4628 from Nissen and Schuster 2010 ([1]) and Nissen and Schuster 2011 ([2]).

Chemical abundances [dex]	Equivalent widths (ours)	Synthesis (ours)	Synthesis (NS10)	NS10/NS11
[Mg `I`/Fe]	0.17	0.26 ± 0.16	0.17 ± 0.16	0.13 ± 0.04 [1]
[Si `I`/Fe]	0.15	0.23 ± 0.23	0.15 ± 0.22	0.19 ± 0.04 [1]
[Ca `I`/Fe]	0.31 ± 0.04	0.41 ± 0.09	0.29 ± 0.08	0.31 ± 0.02 [1]
[Ba `II`/Fe]	-0.01 ± 0.03	-0.52 ± 0.10	-0.58 ± 0.10	-0.16 ± 0.04 [2]

Table 5.4: Chemical abundances estimated from `Blue 1` and `Blue 2` using the equivalent width method and the synthetic spectral fitting technique on the corresponding spectral lines reported in Appendix A. Both methods were performed with the atmospheric parameters of CD-51 4628 reported in Nissen and Schuster 2010. The 'Literature' column represents chemical abundances of CD-51 4628 from the following papers: Nissen and Schuster 2010 ([1]), Nissen and Schuster 2011 ([2]), Mashonkina et al. 2004 ([3]) and Mashonkina et al. 2003 ([4]).

Chemical abundances [dex]	`Blue 1` (EWs)	`Blue 1` (Synthesis)	`Blue 2` (EWs)	`Blue 2` (Synthesis)	Literature
[Na I/Fe]	-0.25	-0.18 ± 0.07	-0.24	-0.18 ± 0.06	-0.26 ± 0.04 [1]
[Mg I/Fe]	-0.04 ± 0.34	0.01 ± 0.01	-0.04 ± 0.34	0.03 ± 0.01	0.13 ± 0.04 [1]
[Si I/Fe]	0.62 ± 0.84	0.17 ± 0.02	0.65 ± 0.87	0.18 ± 0.02	0.19 ± 0.04 [1]
[Ca I/Fe]	0.28 ± 0.91	0.28 ± 0.01	0.28 ± 0.90	0.30 ± 0.01	0.31 ± 0.02 [1]
[Ti I/Fe]	0.45 ± 1.19	0.20 ± 0.01	0.56 ± 1.17	0.23 ± 0.01	0.24 ± 0.02 [1]
[Fe I/H]	-1.39 ± 0.82	-1.48 ± 0.00	-1.36 ± 0.84	-1.46 ± 0.00	-1.30 ± 0.04 [1]
[Fe II/H]	-1.16 ± 0.89	-1.34 ± 0.01	-1.13 ± 0.90	-1.32 ± 0.01	
[Ni I/Fe]	-0.12 ± 0.97	-0.13 ± 0.01	-0.10 ± 0.89	-0.12 ± 0.01	-0.10 ± 0.01 [1]
[Y II/Fe]	-0.08 ± 0.13	0.04 ± 0.04	-0.06 ± 0.14	0.08 ± 0.04	-0.11 ± 0.04 [2]
[Ba II/Fe]	-0.05	-0.05 ± 0.21	-0.06	-0.06 ± 0.22	-0.16 ± 0.04 [2]
[La II/Fe]	0.32 ± 0.01	0.35 ± 0.10	0.37 ± 0.02	0.41 ± 0.10	
[Nd II/Fe]	0.82	0.73 ± 0.11	0.93	0.81 ± 0.10	0.23 ± 0.03 [3]
[Eu II/Fe]	0.88	0.56 ± 0.09	0.88	0.55 ± 0.09	0.54 ± 0.06 [4]

Table 5.5: Chemical abundances estimated from `Blue 1` and `Blue 2` in their Balmer continuum regions (∼330 - 370 nm) using the equivalent width method and the synthetic spectral fitting technique on the corresponding spectral lines reported in Appendix A. Both methods were performed with the atmospheric parameters of CD-51 4628 reported in Nissen and Schuster 2010. The 'Literature' column represents the chemical abundances of CD-51 4628 from Nissen and Schuster 2010 ([1]) and Nissen and Schuster 2011 ([2]).

Chemical	`Blue 1`		`Blue 2`		NS10/NS11
abundances [dex]	(EWs)	(Synthesis)	(EWs)	(Synthesis)	
[Na I/Fe]	-0.25	-0.18 ± 0.07	-0.24	-0.18 ± 0.06	-0.26 ± 0.04 [1]
[Mg I/Fe]	-0.04 ± 0.22	0.32 ± 0.03	-0.02 ± 0.22	0.35 ± 0.03	0.13 ± 0.04 [1]
[Ca I/Fe]	0.35 ± 0.34	0.32 ± 0.04	0.38 ± 0.32	0.28 ± 0.04	0.31 ± 0.02 [1]
[Ti I/Fe]	0.27 ± 0.26	-0.07 ± 0.02	0.30 ± 0.29	-0.05 ± 0.02	0.24 ± 0.02 [1]
[Fe I/H]	-1.49 ± 0.52	-1.60 ± 0.00	-1.46 ± 0.55	-1.59 ± 0.00	-1.30 ± 0.04 [1]
[Fe II/H]	-1.24 ± 0.36	-1.35 ± 0.02	-1.23 ± 0.43	-1.35 ± 0.02	
[Ni I/Fe]	-0.25 ± 0.49	-0.16 ± 0.01	-0.24 ± 0.50	-0.14 ± 0.01	-0.10 ± 0.01 [1]
[Y II/Fe]	-0.11 ± 0.32	-0.17 ± 0.03	-0.10 ± 0.32	-0.16 ± 0.03	-0.11 ± 0.04 [2]
[La II/Fe]	0.29	0.09 ± 0.23	0.36	0.17 ± 0.20	

Chapter 6

Discussion

In this chapter, the stellar atmospheric parameters and chemical abundances of CD-51 4628 listed in the preceding chapter are examined and compared to results from literature whenever possible. For what concerns the abundance analysis, the results obtained with the equivalent width method and the synthetic spectral fitting technique will be compared with one another in order to ascertain whether one method is more accurate and precise than the other when considering the results from abundance analyses found in literature (Mashonkina et al. 2003; Mashonkina et al. 2004; Nissen and Schuster 2010; Nissen and Schuster 2011). Then, the extragalactic origin of CD-51 4628 will be discussed in the context of the abundances obtained with our methods and suggestions for further research are presented.

6.1 Comparisons with Literature

Following the processing of the raw data (see Section 4.3), we have computed the average radial velocity of CD-51 4628 to be 192.1 ± 0.2 km/s using the radial velocities presented in Table 4.4 (Klein-Douwel 2019). Nissen and Schuster 2010 report a (heliocentric) radial velocity of 197.9 km/s for CD-51 4628, which indicates a percentage difference of approximately 3%. However, if we consider the barycentric velocity in `iSpec` to also include the heliocentric velocity then the correction of 5.67 km/s to our radial velocity of CD-51 4628 yields a velocity of ∼197.8 ± 0.2 km/s such that Nissen & Schuster's radial velocity is within one standard deviation (1-σ).

Regarding the determinations of CD-51 4628's atmospheric parameters presented in Table 5.1, we can observe that the results from the second and fourth column have an average percentage difference of 3-4% compared to the atmospheric parameters reported in Nissen and Schuster 2010 and most literature values are within 1-σ to 2-σ of our results with the exception of the effective temperature. The relatively small differences can be a consequence of forcing ionization balance and excitation equilibrium while determining the atmospheric parameters, although these assumptions are imposed in Nissen and Schuster 2010 as well. The offsets might also be due to the use of different neutral and ionized iron lines, since our iron lines have not been cross-referenced with the iron lines from Table 3 in Nissen and Schuster 2011.

It should be noted an offset in the metallicity can be more easily accounted for than an offset in the effective temperature during an abundance analysis. For instance, an offset in [Fe/H] of -0.06 compared to the value reported in Nissen and Schuster 2010 can be accounted for by adding the offset to our results (i.e., as if the results were determined using the same metallicity). Alternatively, we can compute

$$[\mathrm{X/H}] = [\mathrm{X/Fe}] + [\mathrm{Fe/H}] \tag{6.1}$$

which represents a differential abundance of an element X with respect to hydrogen, and therefore nullifies the effect of an offset in the metallicity utilized during the abundance analysis (Maciel 2015). The influence of an offset in the effective temperature on the (differential) abundances is more difficult to ascertain, thus we favor the set of parameters in which the effective

temperature is the closest to the value from Nissen and Schuster 2010. Hence, the results in the fourth column of Table 5.1 are labeled as our preferred values of CD-51 4628's atmospheric parameters obtained with `iSpec`. The negative trend of the excitation potential slope from `RedL`'s second run (shown in Figure 5.1b) is comparable to the findings of Hawkins et al. 2016, which reports an effective temperature of $T_{\text{eff}} = 6223 \pm 100$ K using photometry and a surface gravity of 4.19 ± 0.19 from fitting CD-51 4628's stellar parameters to stellar evolutionary tracks, and could indicate that the microturbulence velocity is overestimated (Blanco-Cuaresma et al. 2014a).

Comparing the second and third columns of Table 5.2 and Table 5.3, we can observe that the chemical abundances obtained with the synthetic spectral fitting technique are higher than those obtained with the equivalent width method by approximately 0.10 dex when inputting the same atmospheric parameters, with the exception of [Ba `II`/Fe]. This difference can be due to the synthetic spectral fitting technique generally being more accurate than the equivalent width method. Taking into account the offset of -0.06 between the metallicities used for the third and fourth columns of Tables 5.2-3, most results agree within 1-σ except for [Ti `I`/Fe] and [Ni `I`/Fe]. A possible explanation might be that the Ti `I` and Ni `I` lines are more sensitive to changes in the input stellar atmospheric parameters (e.g., T_{eff} and/or v_{mic}) than the other spectral lines (Sokal et al. 2018).

Regarding the literature values, the chemical abundances reported in Nissen and Schuster 2010; Nissen and Schuster 2011 are largely within 1-σ to 2-σ of the results listed in the fourth columns of Tables 5.2-3, which means that the atmospheric parameters from Nissen and Schuster 2010 can be safely utilized in the blue. However, [Ba `II`/Fe] deviates significantly from the literature value and is considered an outlier in our data. Figure 6.1 shows the corresponding Ba `II` lines in `RedU` and the synthetic spectrum which was generated. Since the spectral lines in `RedU` and the synthetic spectrum do not match well, it is likely that this has resulted in an underestimated [Ba `II`/Fe] abundance even though the Ba `II` lines are fitted relatively well in the original spectrum. Then, averaging the α abundances obtained with synthesis in the red (from the fourth columns of Tables 5.2-3) gives us $[\alpha/\text{Fe}] \approx 0.20 \pm 0.08$ for CD-51 4628 which coincides with the α-enhancement reported in Nissen and Schuster 2010 within 1-σ.

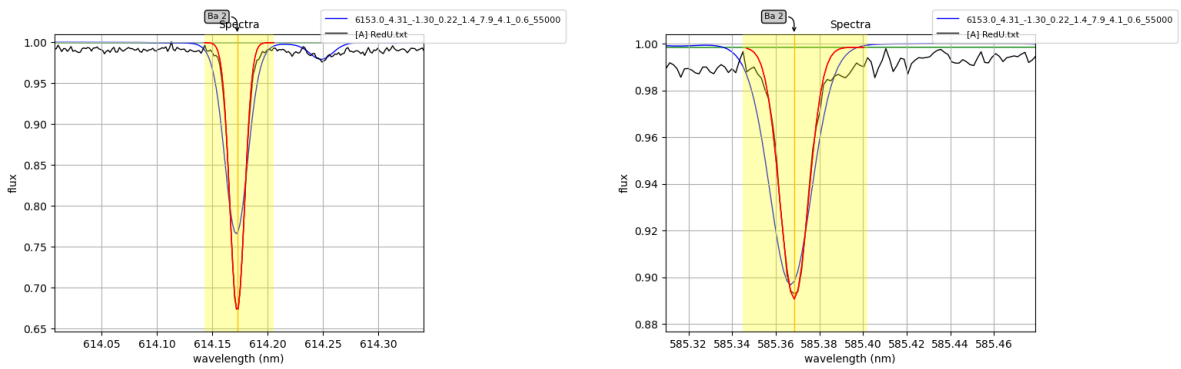

Figure 6.1: Plots of the two Ba II lines in `RedU` (black) and the generated synthetic spectrum (blue) at (a) 585.4 nm and (b) 614.2 nm, with the flux in normalized units on the y-axis and the wavelength in nanometers on the x-axis. Following the shape of the spectral lines, the red lines in the yellow shaded regions are the fitted Gaussian models. These plots are made with `iSpec`.

Comparing the chemical abundances obtained from `Blue 1` and `Blue 2` (see Table 5.4) with the equivalent width method (columns 2 and 4) and the synthetic spectral fitting technique (columns 3 and 5), the results largely agree with each other within 1-σ to 2-σ when there are uncertainties reported on the abundances. It appears that a slight modification in a continuum fit does not significantly affect the outcome of an abundance analysis, although care must of course be taken to ensure a good continuum fit when normalizing any spectrum.

In Table 5.4, the chemical abundances obtained with synthesis are overall more precise (and accurate) than the ones obtained with equivalent widths, except for [La `II`/Fe]. The literature values are within 1-σ to 2-σ of our 'synthesis results', with the exception of [Mg `I`/Fe], [Fe `I`/H], [Y `II`/Fe] and [Nd `II`/Fe] (Mashonkina et al. 2003; Mashonkina et al. 2004; Nissen and Schuster 2010; Nissen and Schuster 2011). The Mg `I` and Fe `I` lines could not be cross-referenced with line data from literature, and some of their lines might then not be good lines for an abundance analysis. Four of the Y `II` lines, encompassing a wavelength range of 377.4 - 395.0 nm, are within the region of the Balmer jump (where the continuum is challenging to fit). The Nd `II` line at 410.9 nm is blended with the outer edge of the H-δ line, which could have negatively influenced the result of [Nd `II`/Fe]. It should be noted that other (slight) deviations from the literature values could be explained by the use of a different solar abundance table and/or radiative transfer code, since Nissen and Schuster 2010 utilized the Uppsala EQWIDTH program.

The following chemical abundances estimated from `Blue 1` and `Blue 2` in the Balmer continuum region (see Table 5.5) differ significantly from the results in Table 5.4: [Mg `I`/Fe] (synthesis), [Ti `I`/Fe], [Fe `I`/H], [Ni `I`/Fe] (equivalent widths) and [La `II`/Fe] (synthesis). Regarding [Mg `I`/Fe] and [La `II`/Fe], the generated synthetic spectra appear to be a poor fit to the normalized blue spectra. As an example, Figure 6.2 presents the La `II` line at 333.8 nm and the synthetic spectrum clearly does not follow the shape of `Blue 1` near this line. The differences in [Ti `I`/Fe] and [Fe `I`/H] can be due to the "Balmer Dip" effect: the abundances of Ti `I`, Ti `II` and Fe `I` are lowered by $\sim$0.08 - 0.27 dex in the Balmer continuum region while the Fe `II` abundances might increase in this region for some stars (which we can also observe, although the effect is not nearly as evident) (Roederer et al. 2018a; Roederer et al. 2018b). The Balmer Dip effect is most likely due to 3D and/or non-LTE effects which are unaccounted for in an 1D LTE abundance analysis, i.e. these simplifying approximations might be breaking down in the Balmer continuum (Lawler and Den Hartog 2018). In the case of [Ni `I`/Fe], the inaccuracy of the equivalent width method in the heavily blended Balmer continuum region might be the cause of the significant deviation.

Lastly, Table 6.1 and Figure 6.3 present our preferred results for the chemical abundances of CD-51 4628 in the blue. We have averaged the results from the third and fifth column of Table 5.4, since the abundances obtained with the synthetic spectral fitting technique are generally more precise than the ones obtained with the equivalent width method and these results all have an associated uncertainty (even when there is only one spectral line). Furthermore, Blanco-Cuaresma 2019 described that the mixing of results from equivalent widths and synthesis is not a recommended practice. However, the abundances of Mg `I`, Y `II` and Nd `II` are not reliable estimates given our previous concerns regarding the spectral lines which were used for the abundance analysis. The α-enhancement is computed to be $[\alpha/\mathrm{Fe}] \approx 0.18 \pm 0.01$ when including the result for [Mg `I`/Fe] and $[\alpha/\mathrm{Fe}] \approx 0.23 \pm 0.01$ when considering only [Si `I`/Fe], [Ca `I`/Fe] and [Ti `I`/Fe], which is within 1-σ of the α-enhancement from Nissen and Schuster 2010. In Figure Figure 6.4, we have roughly pinpointed $[\alpha/\mathrm{Fe}] \approx 0.18 \pm 0.01$ onto Figure 1 from Nissen and Schuster 2010, in which the open blue symbols are the high-α stars and the filled red symbols

the low-α stars.

Thus, our original aim of determining new s- and r-process elements in CD-51 4628 is achieved. However, the abundances of Os `I` and Th `II` could not be ascertained since their spectral lines were too weak and/or too blended for properly determining the associated abundances. Regarding Os `I`, when generating synthetic spectra with increasingly higher fixed abundances of Os `I` the synthetic shape of the spectral line at 432.9 nm (Figure 4.4a) followed the continuum flow (i.e., did *not* follow the shape of a 'normal' absorption line) which could indicate that this line is a bad line for an abundance analysis.

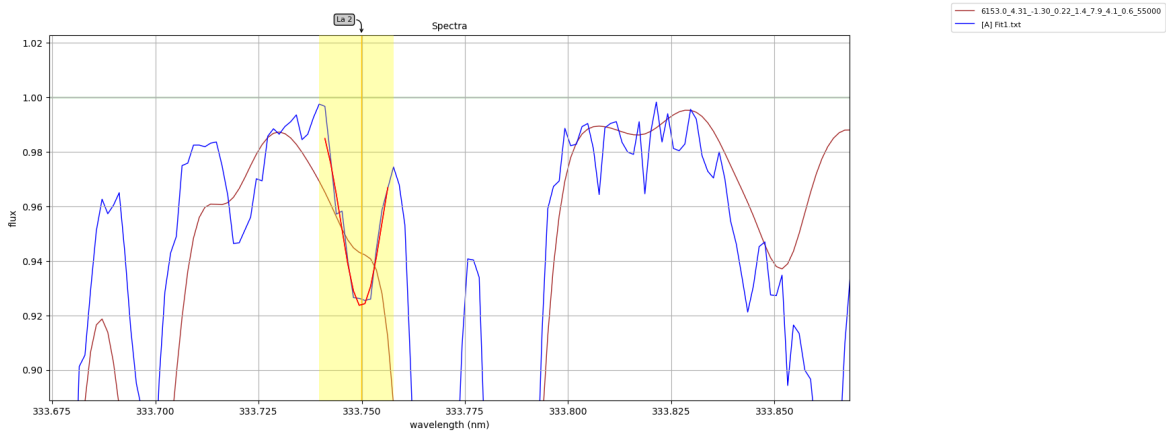

Figure 6.2: Plot of the La `II` line at 333.8 nm in `Blue 1` (blue) and the generated synthetic spectrum (orange), with the flux in normalized units on the y-axis and the wavelength in nanometers on the x-axis. Following the shape of the spectral line, the red line in the yellow shaded regions is the fitted Gaussian model. This plot is made with `iSpec`.

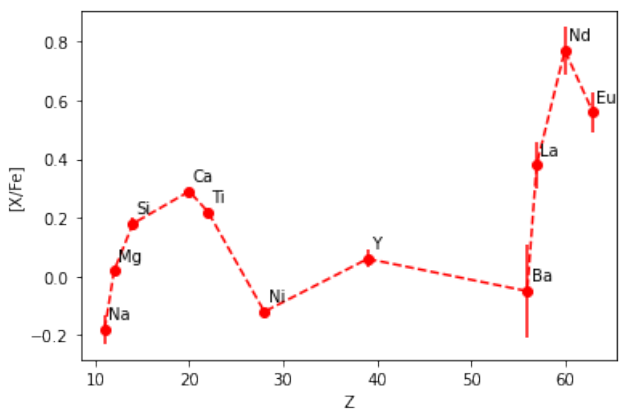

Figure 6.3: Plot of the differential abundance ratios of the chemical elements presented in Table 6.1, except for [Fe `I`/H] and [Fe `II`/H], with [X/Fe] in units of dex on the y-axis and the atomic number Z on the x-axis. X represents the annotated chemical element of a data point.

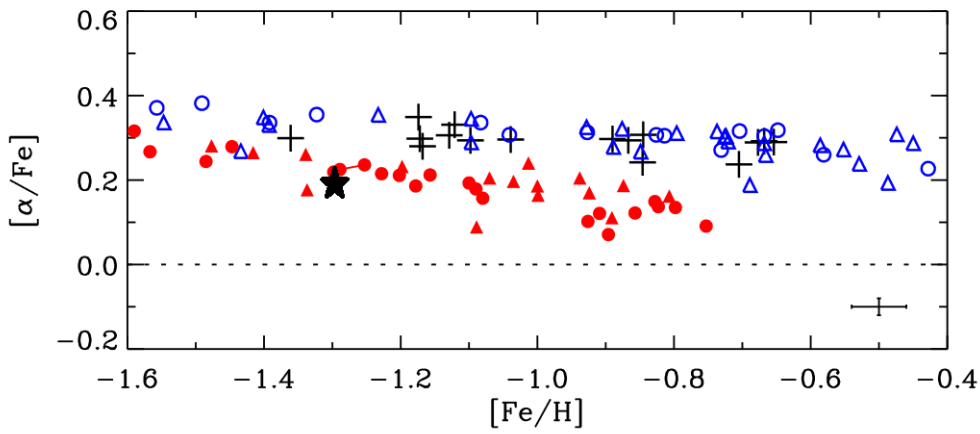

Figure 6.4: Plot of the α-enhancement [α/Fe] on the y-axis and the metallicity [Fe/H] on the x-axis for low-α (filled red symbols), high-α (open blue symbols) and thick-disk (crosses) stars. Halo stars with UVES spectra are indicated by circles and with FIES spectra by triangles. CD-51 4628 is depicted as a black star in the plot. This plot comes from Nissen and Schuster 2010.

6.2 Extragalactic Origin of CD-51 4628

Skúladóttir et al. 2020 analyzed 98 stars with -2.4 < [Fe/H] < -0.9 from the Sculptor dwarf spheroidal galaxy in order to investigate the build-up of the neutron-capture elements Y, Ba, La, Nd and Eu at low metallicity. Plotting the differential abundances of [La/Ba] and [Eu/Ba] against [Ba/H], it is possible to discern the abundance trends of Sculptor and Milky Way stars as shown in Figure 6.5. The black and white squares represent Milky Way stars, and the Sculptor stars from the sample of Skúladóttir et al. 2020 are represented by blue and light-blue circles. The blue circles represent stars observed with FLAMES/GIRAFFE and the light-blue circles those observed with FLAMES/UVES. Abundance measurements of Sculptor stars from other literature sources are represented by magenta diamonds, and open diamonds indicate stars with peculiar abundances of the neutron-capture elements. By roughly pinpointing our data from Table 6.1 onto these plots (as a red star), we can observe that CD-51 4628 mainly fits into the abundance trends of Sculptor stars. However, due to frequent overlap of Sculptor and Milky Way stars it is difficult to ascertain exactly which of the depicted abundance trends CD-51 4628 would fit into more.

Matsuno et al. 2021 analyzed 76 Gaia-Enceladus stars and 81 in-situ stars from the Milky Way in order to comprehend the origin of r-process elements in Gaia-Enceladus. The chemical abundances of the stars were taken from GALAH DR3. Plotting the differential abundances of [Mg/Fe], [Eu/Mg], [Ba/Eu] and [La/Eu] against [Fe/H], it is possible to distinguish the abundance trends of the Gaia-Enceladus stars and the in-situ stars as shown in Figure 6.6. The orange dots represent Gaia-Enceladus stars and the blue squares in-situ stars. The green squares, the red squares and the purple triangles correspond to Fornax, Sagittarius and the Large Magellanic Cloud (LMC) which are satellite dwarf galaxies of the Milky Way (Matsuno et al. 2021). By roughly pinpointing our data from Table 6.1 onto these plots (as a black star), we can observe that CD-51 4628 fits into the abundance trends of the Gaia-Enceladus stars and Fornax in the upper two panels and into the trends of Fornax in the lower panels. When considering the estimate of [Mg I/Fe] = 0.17 ± 0.16 in the red, these observations remain approximately valid.

Table 6.1: Chemical abundances of CD-51 4628 in the blue, obtained by averaging the results from the third and fifth column of Table 5.4.

Chemical abundances [dex]	Value
[Na I/Fe]	-0.18 ± 0.05
[Mg I/Fe]	0.02 ± 0.01
[Si I/Fe]	0.18 ± 0.02
[Ca I/Fe]	0.29 ± 0.01
[Ti I/Fe]	0.22 ± 0.01
[Fe I/H]	-1.47 ± 0.00
[Fe II/H]	-1.33 ± 0.01
[Ni I/Fe]	-0.12 ± 0.01
[Y II/Fe]	0.06 ± 0.03
[Ba II/Fe]	-0.05 ± 0.16
[La II/Fe]	0.38 ± 0.08
[Nd II/Fe]	0.77 ± 0.08
[Eu II/Fe]	0.56 ± 0.07

Thus, our findings support the scenario in which the Milky Way merged with low-mass dwarf galaxies at an earlier time in its history, as described in Section 2.1.

6.3 Suggestions for Further Research

In order to obtain reliable chemical abundances, we have to rely heavily on a good line selection of spectral lines as deduced from the examples presented in Figure 6.1 and Figure 6.2. Since line lists from other authors can contain lines which are considered 'bad' in our spectra (e.g., lines which are blended in our spectra), it is recommended to check the Gaussian and synthetic fits of the lines in `iSpec` and decide in a homogeneous manner whether a line should be left out from the abundance analysis. Unfortunately, there is not much line data available for warm dwarf stars when determining abundances of lighter, iron-peak and neutron-capture elements in the blue and specifically in the Balmer continuum region. For subsequent analyses, it is recommended to experiment with processing a spectrum section by section as opposed to normalizing and treating the whole spectrum in a single attempt.

As suggested by Blanco-Cuaresma 2019, the effect of different radiative transfer codes (e.g., `Turbospectrum`, `SPECTRUM`, etc.) on our determinations of the atmospheric parameters and the chemical abundances should be ascertained in order to ensure the consistency of our results. It should be noted that we chose to utilize `MOOG` when applying the synthetic spectral fitting technique such that the radiative transfer code is consistent with `MOOG` EW used in the equivalent width method.

Finally, in order to investigate the heritage of CD-51 4628 more extensively in the context of s- and r-process production sites, it is recommended to extend the list of s- and r-process elements and make a greater effort to obtain abundances of heavy r-process elements such as Os `I` and Th `II`, or at least upper limits on their abundances by means of a precise and accurate synthesis.

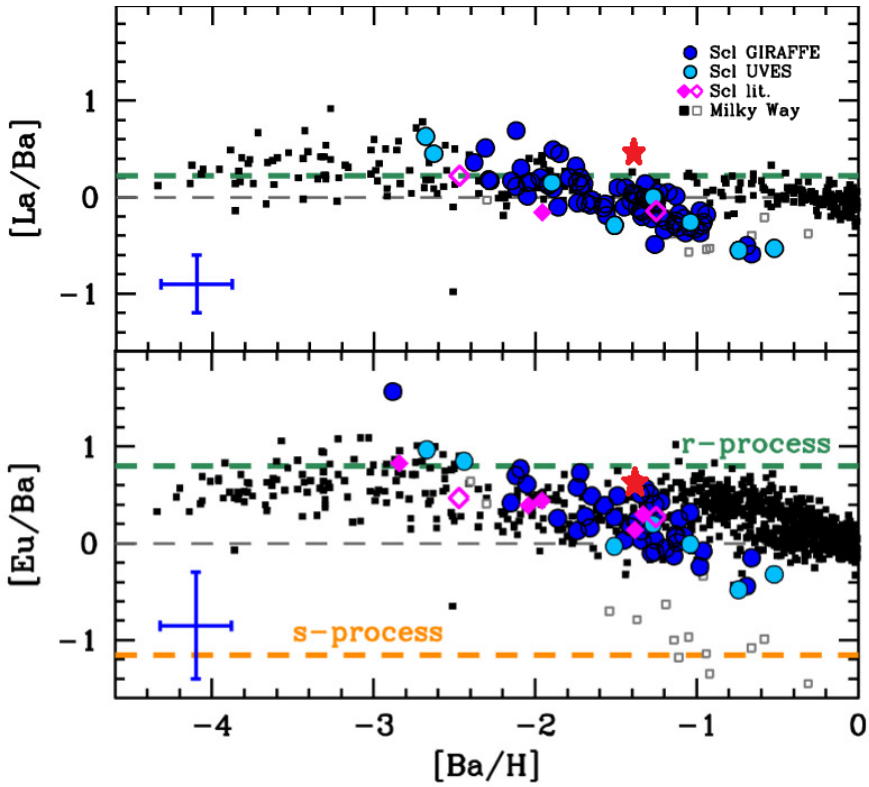

Figure 6.5: Plots of the abundance trends of Sculptor stars (light-blue/blue dots and magenta diamonds) and Milky Way stars (black and white squares). The green and orange dashed lines represent the abundance ratio of [Eu/Ba] of the pure r- and s-process, respectively. CD-51 4628 is depicted as a red star in the plots. These plots come from Skúladóttir et al. 2020.

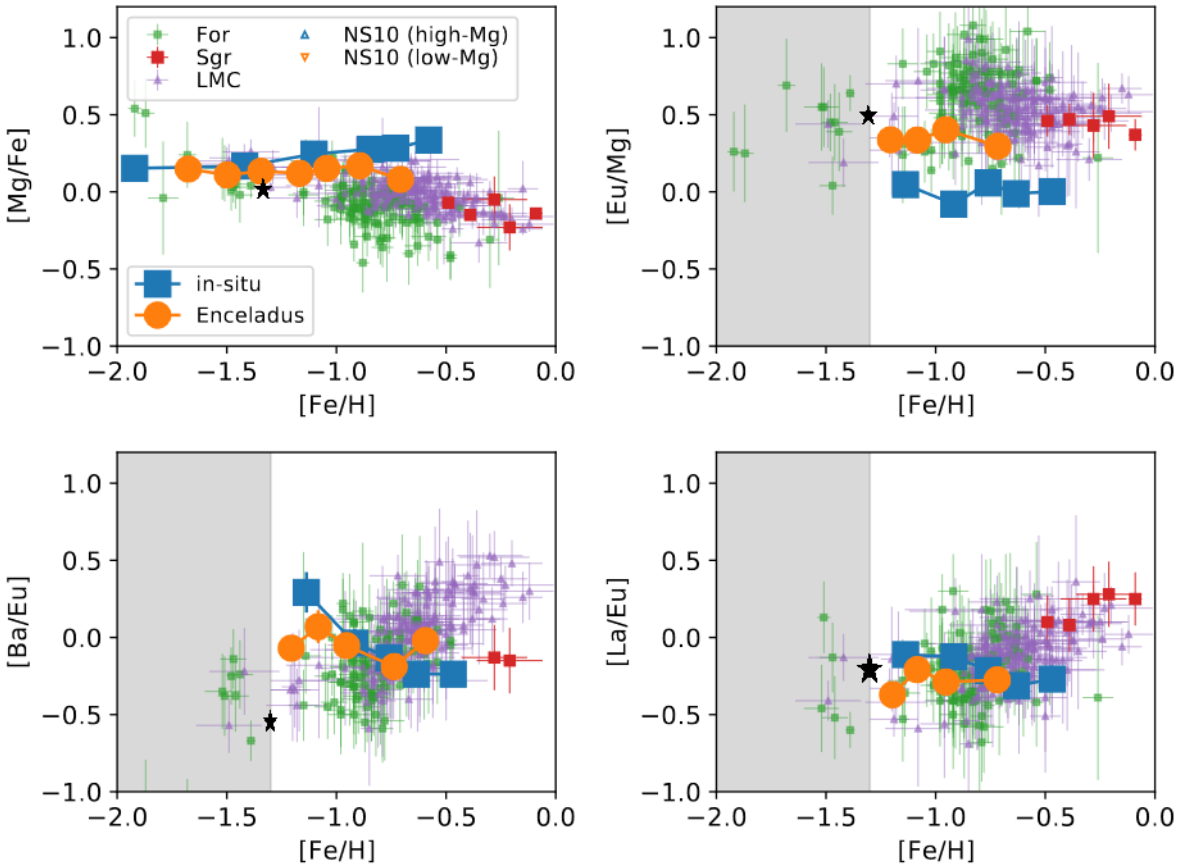

Figure 6.6: Plots of the abundance trends of Gaia-Enceladus stars (orange dots), in-situ stars (blue squares), Fornax (green squares), Sagittarius (red squares) and the Large Magellanic Cloud (purple triangles). CD-51 4628 is depicted as a black star in the plots, and the gray area corresponds to a metallicity range of $-2 < [\mathrm{Fe/H}] < -1.3$ in which the abundance of europium could not be reliably interpreted. These plots come from Matsuno et al. 2021.

Chapter 7

Conclusion

In this thesis, we have performed an extensive abundance analysis of the low-α halo star CD-51 4628, which included determining its stellar atmospheric parameters, using blue and red high-resolution UVES absorption line spectra[1]. To this end, the equivalent width method and the synthetic spectral fitting technique were applied to the normalized spectra of CD-51 4628 making use of the spectroscopic software framework `iSpec`. Comparing the results from our abundance analysis to the literature values of Mashonkina et al. 2003; Mashonkina et al. 2004; Nissen and Schuster 2010 and Nissen and Schuster 2011, we have found that our results generally agree within 1-σ to 2-σ to the literature values and we have verified the α-enhancement of CD-51 4628 reported in Nissen and Schuster 2010. Additionally, we have shown that the synthetic spectral fitting technique produces more accurate and precise results than the equivalent width method overall, as previously described by Blanco-Cuaresma 2019 as well.

Using absorption lines from the Balmer continuum region ($\sim$330 - 370 nm), we have found significant deviations in the abundances of Ti `I` and Fe `I` when compared to the chemical abundances obtained with lines from the whole spectrum. These anomalies might be due to the 'Balmer Dip' effect which has appeared to lower the abundances of Ti `I`, Ti `II` and Fe `I` in the Balmer continuum region according to Roederer et al. 2018b. Due to the prominent Balmer jump in the blue spectra of CD-51 4628, the Gaussian models and synthetic spectra fitted to the spectral lines in this region should be carefully examined for the abnormalities mentioned in this thesis (which also serves as a general recommendation for any future abundance analysis).

We have compared the abundance ratios [La/Ba], [Eu/Ba], [Mg/Fe], [Eu/Mg] and [Ba/Eu] of CD-51 4628 to literature values of Gaia-Enceladus stars, Galactic in-situ stars and stars from the satellite dwarf galaxies Sculptor, Fornax, Sagittarius and LMC (Matsuno et al. 2021; Skúladóttir et al. 2020). As Nissen and Schuster 2010 suggested, CD-51 4628 is most likely accreted from a satellite dwarf galaxy with a different star formation history than the Milky Way since its chemical abundances appear to roughly fit into the abundance trends of Gaia-Enceladus stars and stars from the dwarf galaxies Fornax and Sculptor. These findings support the hierarchical galaxy formation scenario, although we are merely considering one low-α star as opposed to a larger sample of low-α stars (Schlaufman et al. 2009).

Suggestions for further research would then be to study a larger sample of low-α stars in order to inspect whether this stellar population would indeed follow the abundance trends of extragalactic stellar systems, and in particular Gaia-Enceladus, and to extend the list of heavy s- and r-process elements used in a future abundance analysis. To this end, considerable effort should be made to obtain a homogeneous line list for blue stellar spectra (i.e., < 420 nm).

[1] `Blue`, `Blue 1`, `Blue 2`, `RedL`, `RedU` and the normalized spectra of `RedL` and `RedU` are available via https://github.com/IHarmers/BachelorThesis_Spectra-iSpec-.

Acknowledgements

Many thanks to my supervisor Prof. Dr. Eline Tolstoy for her abundant enthusiasm, patience and help during this project and particularly with figuring out how iSpec functions as a spectroscopic software framework (which is still a work in progress). Additionally, many thanks to my family and Heine Jan Lindemulder for their continued support during long days of staring at a computer screen. Based on observations collected at the European Southern Observatory under ESO programme 67.D-0086(A).

Bibliography

Arcones, A., & Montes, F. (2011). PRODUCTION OF LIGHT-ELEMENT PRIMARY PROCESS NUCLEI IN NEUTRINO-DRIVEN WINDS. *ApJ*, *731*(1), 5. https://doi.org/10.1088/0004-637X/731/1/5

Asplund, M., Grevesse, N., Sauval, A. J., & Scott, P. (2009). The Chemical Composition of the Sun. *Annual Review of Astronomy and Astrophysics*, *47*(1), 481–522. https://doi.org/10.1146/annurev.astro.46.060407.145222

Aufdenberg, J. P. (2003). Stellar spectroscopy. In R. A. Meyers (Ed.), *Encyclopedia of physical science and technology (third edition)* (pp. 15–44). Academic Press. https://doi.org/10.1016/B0-12-227410-5/00735-3

Bakker, A., & Gravemeijer, K. P. E. (2006). An Historical Phenomenology of Mean and Median. *Educational Studies in Mathematics*, *62*(2), 149–168. https://doi.org/10.1007/s10649-006-7099-8

Blanco-Cuaresma, S. (2019). Modern stellar spectroscopy caveats. *Monthly Notices of the Royal Astronomical Society*, *486*, 2075–2101. https://doi.org/10.1093/mnras/stz549

Blanco-Cuaresma, S., Soubiran, C., Heiter, U., & Jofré, P. (2014a). Determining stellar atmospheric parameters and chemical abundances of FGK stars with iSpec. *A&A*, *569*, A111. https://doi.org/10.1051/0004-6361/201423945

Blanco-Cuaresma, S., Soubiran, C., Jofré, P., & Heiter, U. (2014b). The Gaia FGK benchmark stars. High resolution spectral library. *Astronomy and Astrophysics*, *566*, A98. https://doi.org/10.1051/0004-6361/201323153

Bland-Hawthorn, J., & Gerhard, O. (2016). The Galaxy in Context: Structural, Kinematic and Integrated Properties. *Annu. Rev. Astron. Astrophys.*, *54*(1), 529–596. https://doi.org/10.1146/annurev-astro-081915-023441

Buder, S., Lind, K., Ness, M. K., Feuillet, D. K., Horta, D., Monty, S., Buck, T., Nordlander, T., Bland-Hawthorn, J., Casey, A. R., De Silva, G. M., D'Orazi, V., Freeman, K. C., Hayden, M. R., Kos, J., Martell, S. L., Lewis, G. F., Lin, J., Schlesinger, K. J., ... Collaboration, T. G. (2022). The GALAH Survey: Chemical tagging and chrono-chemodynamics of accreted halo stars with GALAH+ DR3 and *Gaia* eDR3. *Monthly Notices of the Royal Astronomical Society*, *510*(2), 2407–2436. https://doi.org/10.1093/mnras/stab3504

Burbidge, E. M., Burbidge, G. R., Fowler, W. A., & Hoyle, F. (1957). Synthesis of the Elements in Stars. *Reviews of Modern Physics*, *29*(4), 547–650. https://doi.org/10.1103/revmodphys.29.547

Carollo, D., Beers, T. C., Lee, Y. S., Chiba, M., Norris, J. E., Wilhelm, R., Sivarani, T., Marsteller, B., Munn, J. A., Bailer-Jones, C. A. L., Fiorentin, P. R., & York, D. G. (2007). Two stellar components in the halo of the Milky Way. *Nature*, *450*(7172), 1020–1025. https://doi.org/10.1038/nature06460

Copi, C. J., Schramm, D. N., & Turner, M. S. (1995). Big-Bang Nucleosynthesis and the Baryon Density of the Universe. *Science*, *267*(5195), 192–199. https://doi.org/10.1126/science.7809624

Cyburt, R. H., Fields, B. D., Olive, K. A., & Yeh, T.-H. (2016). Big Bang Nucleosynthesis: 2015. *Rev. Mod. Phys.*, *88*(1), 015004. https://doi.org/10.1103/RevModPhys.88.015004

Deason, A. J., Belokurov, V., Koposov, S. E., & Lancaster, L. (2018). Apocenter Pile-up: Origin of the Stellar Halo Density Break. *ApJL*, *862*(1), L1. https://doi.org/10.3847/2041-8213/aad0ee

Dekker, H., D'Odorico, S., Kaufer, A., Delabre, B., & Kotzlowski, H. (2000). Design, construction, and performance of UVES, the echelle spectrograph for the UT2 Kueyen Telescope at the ESO Paranal Observatory (M. . Iye & A. F. M. Moorwood, Eds.). *SPIE Proceedings*. https://doi.org/10.1117/12.395512

Efstathiou, G., & Jones, B. J. T. (1980). Angular momentum and the formation of galaxies by gravitational instability. *Comments on Astrophysics*, *8*, 169–176.

Freudling, W., Romaniello, M., Bramich, D. M., Ballester, P., Forchi, V., García-Dabló, C. E., Moehler, S., & Neeser, M. J. (2013). Automated data reduction workflows for astronomy. *Astronomy Astrophysics*, *559*, A96. https://doi.org/10.1051/0004-6361/201322494

Gilmore, G., Randich, S., Asplund, M., Binney, J., Bonifacio, P., Drew, J., Feltzing, S., Ferguson, A., Jeffries, R., Micela, G., Negueruela, I., Prusti, T., Rix, H.-W., Vallenari, A., Alfaro, E., Allende-Prieto, C., Babusiaux, C., Bensby, T., Blomme, R., ... Gaia-ESO Survey Team. (2012). The Gaia-ESO Public Spectroscopic Survey. *The Messenger*, *147*, 25–31. https://ui.adsabs.harvard.edu/abs/2012Msngr.147...25G

Gray, R. O., & Corbally, C. J. (1994). The calibration of MK spectral classes using spectral synthesis. 1: The effective temperature calibration of dwarf stars. *The Astronomical Journal*, *107*, 742. https://doi.org/10.1086/116893

Grevesse, N., Asplund, M., & Sauval, A. J. (2007). The Solar Chemical Composition. *Space Sci Rev*, *130*(1), 105–114. https://doi.org/10.1007/s11214-007-9173-7

Gustafsson, B., Edvardsson, B., Eriksson, K., Jørgensen, U. G., Nordlund, Å., & Plez, B. (2008). A grid of MARCS model atmospheres for late-type stars: I. methods and general properties. *A&A*, *486*(3), 951–970. https://doi.org/10.1051/0004-6361:200809724

Hadrava, P. (2006). Disentangling telluric lines in stellar spectra. *Astronomy & Astrophysics*, *448*(3), 1149–1152. https://doi.org/10.1051/0004-6361:20054209

Hansen, C. J. (2022). Heavy Elements – They came out of the blue. *Exp Astron*. https://doi.org/10.1007/s10686-022-09841-0

Hansen, C. J., Andersen, A. C., & Christlieb, N. (2014). Stellar abundances and presolar grains trace the nucleosynthetic origin of molybdenum and ruthenium. *A&A*, *568*, A47. https://doi.org/10.1051/0004-6361/201423535

Hawkins, K., Jofré, P., Heiter, U., Soubiran, C., Blanco-Cuaresma, S., Casagrande, L., Gilmore, G., Lind, K., Magrini, L., Masseron, T., Pancino, E., Randich, S., & Worley, C. C. (2016). Gaia FGK benchmark stars: New candidates at low metallicities. *A&A*, *592*, A70. https://doi.org/10.1051/0004-6361/201628268

Hearnshaw, J. (2009). *Astronomical Spectrographs and their History* (Illustrated). Cambridge University Press.

Heiter, U., Lind, K., Asplund, M., Barklem, P. S., Bergemann, M., Magrini, L., Masseron, T., Mikolaitis, Š., Pickering, J. C., & Ruffoni, M. P. (2015). Atomic and molecular data for optical stellar spectroscopy. *arXiv:1506.06697 [astro-ph]*. https://doi.org/10.1088/0031-8949/90/5/054010

Helmi, A., Babusiaux, C., Koppelman, H. H., Massari, D., Veljanoski, J., & Brown, A. G. A. (2018). The merger that led to the formation of the Milky Way's inner stellar halo and thick disk. *Nature*, *563*(7729), 85–88. https://doi.org/10.1038/s41586-018-0625-x

Hendricks, B., Koch, A., Lanfranchi, G. A., Boeche, C., Walker, M., Johnson, C. I., Peñarrubia, J., & Gilmore, G. (2014). THE METAL-POOR KNEE IN THE FORNAX DWARF SPHEROIDAL GALAXY. *The Astrophysical Journal*, *785*(2), 102. https://doi.org/10.1088/0004-637X/785/2/102

Higl, J., & Weiss, A. (2017). Testing stellar evolution models with detached eclipsing binaries. *A&A*, *608*, A62. https://doi.org/10.1051/0004-6361/201731008

Hill, V., Plez, B., Cayrel, R., Beers, T. C., Nordström, B., Andersen, J., Spite, M., Spite, F., Barbuy, B., Bonifacio, P., Depagne, E., François, P., & Primas, F. (2002). First stars. I. The extreme r-element rich, iron-poor halo giant CS 31082-001: Implications for the r-process site(s) and radioactive cosmochronology. *A&A*, *387*(2), 560–579. https://doi.org/10.1051/0004-6361:20020434

Jofré, P., Heiter, U., & Soubiran, C. (2019). Accuracy and precision of industrial stellar abundances. *Annu. Rev. Astron. Astrophys.*, *57*(1), 571–616. https://doi.org/10.1146/annurev-astro-091918-104509

Klein-Douwel, R. J. H. (2019). *Physics Laboratory 1 Manual 2019 - 2020*. University of Groningen.

Kurucz, R. L. (2005). ATLAS12, SYNTHE, ATLAS9, WIDTH9, et cetera. *Memorie della Societa Astronomica Italiana Supplementi*, *8*, 14.

Lawler, J., & Den Hartog, E. (2018). Improving the Ar I and II branching ratio calibration method: Monte Carlo simulations of effects from photon scattering/reflecting in hollow cathodes. *Journal of Quantitative Spectroscopy and Radiative Transfer*, *207*, 41–47. https://doi.org/10.1016/j.jqsrt.2017.12.010

LeBlanc, F. (2010). *An Introduction to Stellar Astrophysics* (1st ed.). Wiley.

Maciel, W. J. (2015). *Astrophysics of the Interstellar Medium* (2013th ed.). Springer.

Martinou, A., & Bonatsos, D. (2019). Magic numbers of cylindrical symmetry.

Mashonkina, L., Gehren, T., Travaglio, C., & Borkova, T. (2003). Mg, Ba and Eu abundances in thick disk and halo stars. *A&A*, *397*(1), 275–284. https://doi.org/10.1051/0004-6361:20021512

Mashonkina, L. I., Kamaeva, L. A., Samotoev, V. A., & Sakhibullin, N. A. (2004). Neutron-capture elements in halo, thick-disk, and thin-disk stars: Neodymium. *Astronomy Reports*, *48*(3), 185–199. https://doi.org/10.1134/1.1687012

Matsuno, T., Aoki, W., & Suda, T. (2019). Origin of the Excess of High-energy Retrograde Stars in the Galactic Halo. *ApJL*, *874*(2), L35. https://doi.org/10.3847/2041-8213/ab0ec0

Matsuno, T., Hirai, Y., Tarumi, Y., Hotokezaka, K., Tanaka, M., & Helmi, A. (2021). R-process enhancements of gaia-enceladus in galah dr3. *A&A*, *650*, A110. https://doi.org/10.1051/0004-6361/202040227

Nissen, P. E., & Schuster, W. J. (2010). Two distinct halo populations in the solar neighborhood: Evidence from stellar abundance ratios and kinematics. *A&A*, *511*, L10. https://doi.org/10.1051/0004-6361/200913877

Nissen, P. E., & Schuster, W. J. (2011). Two distinct halo populations in the solar neighborhood - II. Evidence from stellar abundances of Mn, Cu, Zn, Y, and Ba. *A&A*, *530*, A15. https://doi.org/10.1051/0004-6361/201116619

Randich, S., Gilmore, G., & Gaia-ESO Consortium. (2013). The Gaia-ESO Large Public Spectroscopic Survey. *The Messenger*, *154*, 47–49.

Robinson, K. (2007). *Spectroscopy: The Key to the Stars: Reading the Lines in Stellar Spectra (The Patrick Moore Practical Astronomy Series)* (2007th ed.). Springer.

Roederer, I. U., Sakari, C. M., Placco, V. M., Beers, T. C., Ezzeddine, R., Frebel, A., & Hansen, T. T. (2018a). The R-Process Alliance: A Comprehensive Abundance Analysis of HD 222925, a Metal-poor Star with an Extreme R-process Enhancement of [Eu/H] = -0.14. *The Astrophysical Journal*, *865*(2), 129. https://doi.org/10.3847/1538-4357/aadd92

Roederer, I. U., Sneden, C., Lawler, J. E., Sobeck, J. S., Cowan, J. J., & Boesgaard, A. M. (2018b). Consistent Iron Abundances Derived from Neutral and Singly Ionized Iron Lines in Ultraviolet and Optical Spectra of Six Warm Metal-poor Stars. *The Astrophysical Journal*, *860*(2), 125. https://doi.org/10.3847/1538-4357/aac6df

Rosswog, S., Korobkin, O., Arcones, A., Thielemann, F.-K., & Piran, T. (2014). The long-term evolution of neutron star merger remnants – I. The impact of r-process nucleosynthesis. *Monthly Notices of the Royal Astronomical Society*, *439*(1), 744–756. https://doi.org/10.1093/mnras/stt2502

Schlaufman, K. C., Rockosi, C. M., Prieto, C. A., Beers, T. C., Bizyaev, D., Brewington, H., Lee, Y. S., Malanushenko, V., Malanushenko, E., Oravetz, D., Pan, K., Simmons, A., Snedden, S., & Yanny, B. (2009). INSIGHT INTO THE FORMATION OF THE MILKY WAY THROUGH COLD HALO SUBSTRUCTURE. i. THE ECHOS OF MILKY WAY FORMATION. *ApJ*, *703*(2), 2177–2204. https://doi.org/10.1088/0004-637X/703/2/2177

Schuster, W. J., Moreno, E., Nissen, P. E., & Pichardo, B. (2012). Two distinct halo populations in the solar neighborhood: III. Evidence from stellar ages and orbital parameters. *A&A*, *538*, A21. https://doi.org/10.1051/0004-6361/201118035

Searle, L., & Zinn, R. (1978). Composition of halo clusters and the formation of the galactic halo. *The Astrophysical Journal*, *225*, 357–379. https://doi.org/10.1086/156499

Skúladóttir, Á., Hansen, C. J., Choplin, A., Salvadori, S., Hampel, M., & Campbell, S. W. (2020). Neutron-capture elements in dwarf galaxies. *Astronomy Astrophysics*, *634*, A84. https://doi.org/10.1051/0004-6361/201937075

Sneden, C., Cowan, J. J., & Gallino, R. (2008). Neutron-Capture Elements in the Early Galaxy. *Annu. Rev. Astron. Astrophys.*, *46*(1), 241–288. https://doi.org/10.1146/annurev.astro.46.060407.145207

Sokal, K. R., Deen, C. P., Mace, G. N., Lee, J. J., Oh, H., Kim, H., Kidder, B. T., & Jaffe, D. T. (2018). Characterizing TW Hydra. *The Astrophysical Journal*, *853*(2), 120. https://doi.org/10.3847/1538-4357/aaa1e4

Stumpff, P. (1980). Two Self-Consistent FORTRAN Subroutines for the Computation of the Earth's Motion. *Astronomy and Astrophysics Supplement*, *41*, 1.

Tennyson, J. (2019). *Astronomical Spectroscopy: An Introduction To The Atomic And Molecular Physics Of Astronomical Spectroscopy (Third Edition)*. Van Haren Publishing.

Van der Swaelmen, M., Barbuy, B., Hill, V., Zoccali, M., Minniti, D., Ortolani, S., & Gómez, A. (2016). Heavy elements Ba, La, Ce, Nd, and Eu in 56 Galactic bulge red giants. *A&A*, *586*, A1. https://doi.org/10.1051/0004-6361/201525709

Van der Walt, S., Colbert, S. C., & Varoquaux, G. (2011). The NumPy Array: A Structure for Efficient Numerical Computation. *Computing in Science Engineering*, *13*(2), 22–30. https://doi.org/10.1109/mcse.2011.37

Venn, K. A., Irwin, M., Shetrone, M. D., Tout, C. A., Hill, V., & Tolstoy, E. (2004). Stellar Chemical Signatures and Hierarchical Galaxy Formation. *AJ*, *128*(3), 1177–1195. https://doi.org/10.1086/422734

Walcher, C. J., Coelho, P. R. T., Gallazzi, A., Bruzual, G., Charlot, S., & Chiappini, C. (2015). Abundance patterns in early-type galaxies: is there a "knee" in the [Fe/H] vs. [α/Fe] relation? *Astronomy Astrophysics*, *582*, A46. https://doi.org/10.1051/0004-6361/201525924

Wanajo, S., Janka, H.-T., & Müller, B. (2011). ELECTRON-CAPTURE SUPERNOVAE AS THE ORIGIN OF ELEMENTS BEYOND IRON. *ApJ*, *726*(2), L15. https://doi.org/10.1088/2041-8205/726/2/L15

Wenger, M., Ochsenbein, F., Egret, D., Dubois, P., Bonnarel, F., Borde, S., Genova, F., Jasniewicz, G., Laloë, S., Lesteven, S., & Monier, R. (2000). The SIMBAD astronomical database - The CDS reference database for astronomical objects. *Astron. Astrophys. Suppl. Ser.*, *143*(1), 9–22. https://doi.org/10.1051/aas:2000332

Wright, J. T., & Kanodia, S. (2020). Barycentric Corrections for Precise Radial Velocity Measurements of Sunlight. *The Planetary Science Journal*, *1*(2), 38. https://doi.org/10.3847/PSJ/ababa4

Appendix A

This appendix contains the line data utilized in `iSpec` during the abundance analysis with the absorption line spectra of CD-51 4628. 'wave_peak', 'wave_base' and 'wave_top' correspond to the peak of the spectral line, the beginning of the yellow shaded line region and the end of the line region. In the column 'note', the element corresponding to the line is indicated. For the sake of clarity, we will only present the spectral lines of which there are less than 20.

Blue 1

wave_peak	wave_base	wave_top	note
330.23803	330.22521	330.24874	Na 1
332.99322	332.97839	333.01299	Mg 1
333.21425	333.19294	333.24000	Mg 1
333.66899	333.64696	333.68987	Mg 1
382.93673	382.87337	382.96473	Mg 1
383.23160	383.18482	383.27756	Mg 1
383.83045	383.77311	383.89076	Mg 1
384.37234	384.35447	384.38769	Mg 1
385.88777	385.86325	385.90339	Mg 1
387.83105	387.82190	387.84128	Mg 1
393.83747	393.81273	393.85979	Mg 1
398.67582	398.64775	398.69205	Mg 1
405.75077	405.70442	405.77917	Mg 1
416.72748	416.70192	416.75313	Mg 1
435.18995	435.18380	435.21840	Mg 1
390.55319	390.51002	390.58062	Si 1
410.29390	410.27921	410.32212	Si 1
332.78863	332.77629	332.80813	Y 2
349.60958	349.59990	349.61236	Y 2
354.90119	354.89032	354.91662	Y 2
358.45311	358.43665	358.45741	Y 2
360.07414	360.05478	360.08801	Y 2
360.19244	360.17936	360.20013	Y 2
361.10528	361.09294	361.13308	Y 2
362.87092	362.85364	362.87994	Y 2
363.31043	363.30212	363.32981	Y 2
377.43385	377.41685	377.45145	Y 2 Hill et al. 2002
378.87017	378.85503	378.90071	Y 2 Hill et al. 2002
381.83422	381.81031	381.85183	Y 2 Hill et al. 2002
395.03569	395.01837	395.04883	Y 2 Hill et al. 2002
439.80192	439.78766	439.81534	Y 2 Hill et al. 2002
413.06580	413.05039	413.07669	Ba 2 Hill et al. 2002
333.74994	333.73970	333.75769	La 2
408.67141	408.65970	408.68323	La 2 Hill et al. 2002
412.32338	412.30984	412.33614	La 2 Hill et al. 2002
410.94634	410.93394	410.96024	Nd 2 Hill et al. 2002
412.97283	412.95488	412.99225	Eu 2 Hill et al. 2002

Blue 2

wave_peak	wave_base	wave_top	note
330.23803	330.22521	330.24874	Na 1
332.99322	332.97839	333.01299	Mg 1

333.21425	333.19294	333.24000	Mg 1
333.66899	333.64696	333.68987	Mg 1
382.93673	382.87337	382.96335	Mg 1
383.23160	383.18482	383.27756	Mg 1
383.83045	383.77311	383.89076	Mg 1
384.37234	384.35586	384.38769	Mg 1
385.88777	385.86325	385.90339	Mg 1
387.83106	387.82190	387.84128	Mg 1
393.83746	393.81273	393.85979	Mg 1
398.67582	398.64775	398.69205	Mg 1
405.75077	405.70442	405.77917	Mg 1
416.72748	416.70192	416.75313	Mg 1
435.18995	435.18380	435.21840	Mg 1
390.55319	390.51002	390.58062	Si 1
410.29389	410.27921	410.32212	Si 1
332.78863	332.77629	332.80813	Y 2
349.60958	349.59990	349.61236	Y 2
354.90119	354.89032	354.91662	Y 2
358.45311	358.43665	358.45741	Y 2
360.07414	360.05478	360.08801	Y 2
360.19244	360.17936	360.20013	Y 2
361.10528	361.09294	361.13308	Y 2
362.87092	362.85364	362.87994	Y 2
363.31043	363.30212	363.32981	Y 2
377.43385	377.41685	377.45145	Y 2 Hill et al. 2002
378.87017	378.85503	378.90071	Y 2 Hill et al. 2002
381.83417	381.81031	381.85183	Y 2 Hill et al. 2002
395.03570	395.01837	395.04883	Y 2 Hill et al. 2002
439.80192	439.78766	439.81534	Y 2 Hill et al. 2002
413.06580	413.05039	413.07669	Ba 2 Hill et al. 2002
333.74994	333.73970	333.75769	La 2
408.67141	408.65970	408.68323	La 2 Hill et al. 2002
412.32339	412.30984	412.33614	La 2 Hill et al. 2002
410.94634	410.93394	410.96024	Nd 2 Hill et al. 2002
412.97283	412.95488	412.99225	Eu 2 Hill et al. 2002

RedL

wave_peak	wave_base	wave_top	note
534.94676	534.91976	534.96404	Ca 1
551.29811	551.27649	551.32215	Ca 1
499.95090	499.93031	499.97597	Ti 1
502.28749	502.26580	502.30731	Ti 1
502.48533	502.46780	502.50239	Ti 1
519.29759	519.27973	519.31985	Ti 1
521.03930	521.01474	521.06732	Ti 1
482.90281	482.88733	482.92330	Ni 1
483.11824	483.09902	483.15574	Ni 1
490.44181	490.42371	490.46245	Ni 1
493.58357	493.56444	493.60318	Ni 1
493.73518	493.71802	493.76091	Ni 1
503.53659	503.51656	503.55530	Ni 1
508.11153	508.09069	508.13773	Ni 1
508.41008	508.39231	508.43243	Ni 1
509.99326	509.97375	510.01249	Ni 1
511.53982	511.52059	511.56210	Ni 1
515.57700	515.56204	515.59663	Ni 1

488.36910	488.35248	488.38846	Y 2
508.74284	508.72437	508.76173	Y 2

RedU

wave_peak	wave_base	wave_top	note
571.10897	571.08174	571.13881	Mg 1
615.51471	615.48261	615.54136	Si 1
616.64430	616.61722	616.67597	Ca 1
616.90478	616.87906	616.92941	Ca 1
616.95597	616.92941	616.99319	Ca 1
585.36835	585.34494	585.40200	Ba 2
614.17245	614.14323	614.20534	Ba 2